

Observing Iceland's Eyjafjallajökull 2010 eruptions with the autonomous NASA Volcano Sensor Web

Ashley Gerard Davies,¹ Steve Chien,¹ Joshua Doubleday,¹ Daniel Tran,¹ Thorvaldur Thordarson,^{2,3} Magnús T. Gudmundsson,³ Ármann Höskuldsson,³ Steinunn S. Jakobsdóttir,⁴ Robert Wright,⁵ and Daniel Mandl⁶

Received 14 November 2012; revised 5 February 2013; accepted 19 February 2013; published 9 May 2013.

[1] Between 24 March and 5 June 2010, the Hyperion hyperspectral imager and Advanced Land Imager (ALI) on NASA's *Earth Observing 1 (EO-1)* spacecraft obtained an unprecedented sequence of 50 observation pairs of the eruptions at Fimmvörðuháls and Eyjafjallajökull, Iceland. This high acquisition rate was possible only through the use of data flow streamlined by using the autonomously operating NASA Volcano Sensor Web (VSW). The VSW incorporates notifications of volcanic activity from multiple sources to retask *EO-1* and process Hyperion data to extract eruption parameters from high spatial and spectral resolution visible and short-wavelength infrared data. Physical changes in eruption style and magnitude were charted as the eruptions ran their course. Rapid data downlink and automatic data-processing algorithms generated a variety of products which are compared with estimates from ground-based observations and post-eruption in situ measurements. Estimates of effusion rate from heat loss measurements underestimate actual effusion rate (while still following broad eruption rate trends) but are closer to in situ estimates for effusive eruptions (Fimmvörðuháls) than explosive, ash-rich eruptions (Eyjafjallajökull). During the later stages of the 2010 eruption, VSW-generated products were rapidly delivered to end-users in Iceland to aid in the assessment of risk and hazard. The success of the VSW led to Icelandic Meteorological Office (IMO) in situ sensors being incorporated into the VSW, and in May 2011 an IMO seismic alert autonomously triggered *EO-1* observations of a new eruption at Grímsvötn volcano. Finally, the VSW demonstrates an autonomy-driven, multi-asset, spacecraft retasking and data processing system that maximizes science return, a desirable capability for future NASA missions.

Citation: Davies, A. G., S. Chien, J. Doubleday, D. Tran, T. Thordarson, M. T. Gudmundsson, Á. Höskuldsson, S. S. Jakobsdóttir, R. Wright, and D. Mandl (2013), Observing Iceland's Eyjafjallajökull 2010 eruptions with the autonomous NASA Volcano Sensor Web, *J. Geophys. Res. Solid Earth*, 118, 1936–1956, doi:10.1002/jgrb.50141.

1. Introduction

[2] The 2010 flank and summit eruptions at the Eyjafjallajökull volcano, Iceland, were of modest size by Icelandic standards and by volume erupted [e.g., Gudmundsson *et al.*, 2012]. With a VEI (Volcano Explosivity Index) of 3, the larger, more explosive summit eruption still places relatively low on the eruption magnitude scale. Nevertheless,

the resulting ash plume from the summit eruption in April 2010 posed a serious threat to aviation and led to the closure of a broad swath of European airspace.

[3] As with all volcanic eruptions, speed is of the essence in order to assess volcanic hazard and risk [Tilling, 1989]. The NASA Volcano Sensor Web (VSW) [Chien *et al.*, 2005a; Davies *et al.*, 2006b] utilizes detections of ongoing volcanic activity, commonly from reports of volcanic plumes or detections of anomalous thermal emission, to autonomously and rapidly retarget a spacecraft in Earth orbit to obtain high spatial and high spectral resolution visible (VIS) and short-wavelength infrared (SWIR) observations of the ongoing volcanic activity. In this way, observations from globe-spanning low spatial resolution instruments can be used to schedule the rapid acquisition of data from high spatial resolution assets that only cover a tiny proportion of Earth's surface every day.

[4] The VSW uses advanced spacecraft autonomy software (the Autonomous Sciencecraft software [ASE]) and automated data processing for optimizing spacecraft responses to notifications of ongoing or imminent volcanic eruptions. From such a notification, an orbiting asset (NASA's *Earth*

¹Jet Propulsion Laboratory, California Institute of Technology, Pasadena, California, USA.

²Earth and Planetary Sciences, School of Geosciences, University of Edinburgh, Edinburgh, United Kingdom.

³Institute of Earth Sciences, University of Iceland, Reykjavik, Iceland.

⁴Icelandic Meteorological Office, Reykjavik, Iceland.

⁵Hawaii Institute of Geophysics and Planetology, University of Hawaii, Honolulu, Hawaii, USA.

⁶Goddard Space Flight Center, Greenbelt, Maryland, USA.

Corresponding author: A. Davies, Jet Propulsion Laboratory, 4800 Oak Grove Drive, Pasadena, CA 91040, USA. (Ashley.Davies@jpl.nasa.gov)

©2013. American Geophysical Union. All Rights Reserved.
2169-9313/13/10.1002/jgrb.50141

Observing 1 [EO-1] spacecraft) can be rapidly retasked to obtain high spatial and spectral resolution observations of the volcano. Data are rapidly downlinked, processed, and analyzed, and the resulting products are quickly disseminated to relevant authorities [Chien *et al.*, 2005a; Davies *et al.*, 2006b].

[5] Taking full advantage of recent improvements in mission operations, resource planning and data processing, EO-1 obtained an unprecedented 50 observation pairs (from the Hyperion hyperspectral imager and Advanced Land Imager [ALI] on EO-1) of Fimmvörðuháls and Eyjafjallajökull between 24 March 2010 and 5 June 2010. This paper charts the evolution of the 2010 eruptions at Eyjafjallajökull volcano, Iceland, as seen by EO-1. We compare estimates of effusion rate from Hyperion radiance data with estimates from observations and measurements on the ground, and we describe, in Appendix B, how in situ sensors on Iceland's volcanoes have been linked into the VSW, thus enabling autonomous and rapid spacecraft triggering from notifications of impending volcanic activity.

2. The 2010 Eruption of Eyjafjallajökull

[6] Eyjafjallajökull volcano, Iceland, is a 1651-m-high central volcano crowned by a 2.5-km-diameter caldera and an icecap covering the slopes above 1000 m elevation [Thordarson and Larsen, 2007]. Eyjafjallajökull is located within the Eastern Volcanic Zone (EVZ), which is a young (<3 Myr) propagating rift extending southwest from the

main axial rift in Iceland (Figure 1). Previous historical eruptions at Eyjafjallajökull include a radial fissure eruption around A.D. 920 and small summit eruptions in A.D. 1612 and A.D. 1821–1823 [Larsen, 1999; Óskarsson, 2009]. In the latter event, a short explosive phase in December 1821 was followed by a yearlong period of intermittent explosive to effusive activity and flooding [e.g., Larsen, 1999].

[7] Eyjafjallajökull erupted from 20 March to 12 April 2010 (a flank eruption) and again from 14 April to 22 May 2010 (a summit eruption). Although the eruptions were of small to moderate size, the ash produced during the latter eruption formed and maintained a 5–10-km-high eruption plume for several days at a time. These columns were subsequently dispersed by a southeasterly-flowing jet stream toward Europe. This ash heavily impacted air travel across much of Western Europe and wrought havoc on the global air transportation system. This eruption highlighted, once again, the need to monitor and quickly react to the onset of new eruptions. As a result of fast action by European meteorological offices and aviation authorities, no airplanes were lost due to the ingestion of volcanic ash.

[8] After a prolonged period of unrest at Eyjafjallajökull, beginning in 1994 and peaking in the early months of 2010 [Sigmundsson *et al.*, 2010], a small flank eruption of alkali-basalt began at 23:30 UT on 20 March 2010 in the region of the Fimmvörðuháls pass, which is the saddle between the Eyjafjallajökull and Mýrdalsjökull volcanoes. This eruption took place along a 300-m-long radial fissure

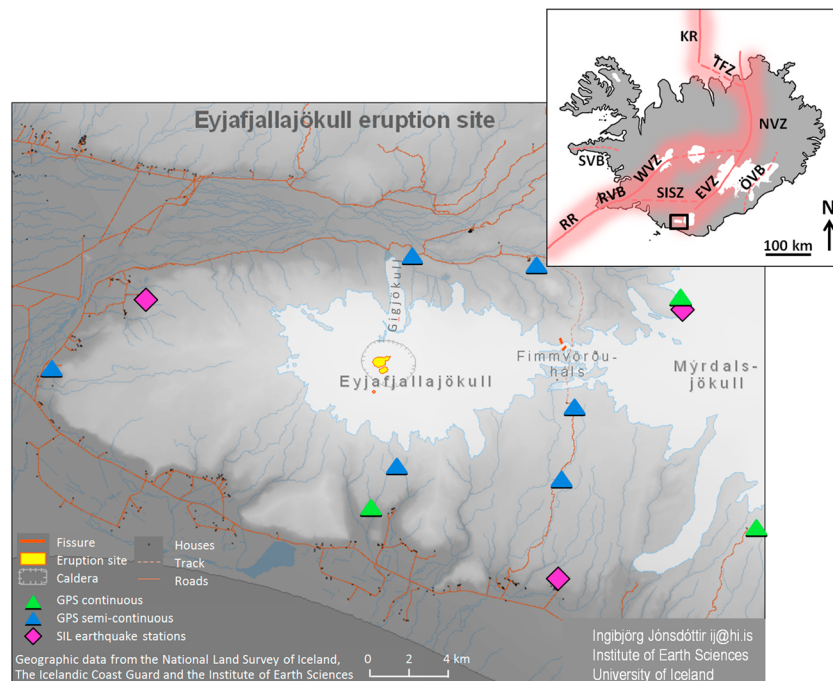


Figure 1. Inset image: tectonic setting of Iceland, showing main volcanic zones (solid lines), fracture zones, and seismic belts (dashed lines). Key: RR=Reykjanes Ridge; RVB=Reykjanes volcanic belt; WVZ=west volcanic zone; SISZ=South Iceland Seismic Zone; EVZ=east volcanic zone; ÖVB=Öræfi volcanic belt; NVZ=north volcanic zone; TFZ=Tjörnes Fracture Zone; KR=Kolbeinsey Ridge; SVB=Snæfellsnes volcanic belt. After Figure 1.2 in Thordarson and Höskuldsson [2006]. Main image: Detail of the 2010 eruption locations, showing the approximate locations of Eyjafjallajökull and the fissures at Fimmvörðuháls. Also shown are the locations of Icelandic Meteorological Office and Institute of Earth Sciences (University of Iceland) sensors which monitor these volcanoes. “SIL” refers to the Iceland National Seismic Network. Image credit: Ingibjörg Jónsdóttir, Institute of Earth Sciences, University of Iceland.

featuring a curtain of fire consisting of 15 lava fountains reaching heights up to 185 m [Edwards *et al.*, 2012; Thordarson *et al.*, 2011]. By 24 March, the fountains were <100 m high, emerging from four vents. On March 31, the activity was characterized by relatively weak fountaining through a forcefully stirring pool of lava. The vents were surrounded by 60- to 80-m-high ramparts, and the level of lava stood at approximately 30 m above the pre-eruption surface. This high stand led to opening of a new fissure trending northwest from the mid-section of the original fissure. As activity on the new fissure intensified, the discharge from the original fissure declined and stopped by 7 April. The lava flow field was dominantly a'a with small domains of pahoehoe and slabby pahoehoe. Advance of lava from the vents was episodic, and lava was discharged from the vents through open channels as well as internal pathways. Open channels were the visible part of the transport system, feeding lava to active a'a flow fronts and producing spectacular lava falls when cascading into nearby gullies. Internal pathways were less conspicuous yet made an important contribution to the overall growth of the flow field, particularly the near-vent sector, as it thickened the lava by inflation and fed significant surface breakouts emerging from apparently stagnant lava sectors. When activity ceased on 12 April, the lava covered 1.3 km². The eruption produced 20×10^6 m³ of basalt, with a mean discharge rate of $10 \text{ m}^3 \text{ s}^{-1}$ [Edwards *et al.*, 2012; Gudmundsson *et al.*, 2012].

[9] Activity then shifted to Eyjafjallajökull. On 14 April 2010, activity began at the summit of Eyjafjallajökull and lasted to 22 May. In total, the summit eruption expelled 0.27 km³ of airborne tephra, smaller amounts of water-transported tephra, and a lava flow. The magma composition was benmoreite to trachyte, and the dense rock equivalent of all of the erupted material was 0.18 km³ [Gudmundsson *et al.*, 2012]. The course of events is described in detail by Gudmundsson *et al.* [2012], and the summary of events given below is based on their work.

[10] On 13 April, an intensive earthquake swarm was detected migrating toward the surface beneath the summit region. The eruption began at ~1:30 UT on 14 April. The eruption can be divided into four distinct phases. The *initial phase* (first explosive phase: see Gudmundsson *et al.* [2012]) (14–18 April) featured phreatomagmatic and magmatic explosions producing ash plumes that reached Europe. The eruption began subglacially, with a substantial portion of the energy of the eruption used for melting the 200-m-thick ice on 14–15 April: ice cauldrons formed, and meltwater drained down the slopes [Magnússon *et al.*, 2012]. Subaerial activity was first detected when a white, steam-loaded eruption plume rose from the summit at 06:00 h UT on 14 April. The steam-rich plume grew during the rest of 14 April. A tephra-laden (dark gray) plume appeared at ~18:30 h UT, by which time the plume had reached an altitude of 9–10 km. Plume-forming activity continued until early on 15 April, producing very fine ash. Ice melting rates were 1000–3000 m³ s⁻¹. Four jökulhlaups subsequently developed with primary discharge down the outlet glacier Gígjökull on the northern flank (Figure 1). The estimated magma eruption rate during this initial phase was $5\text{--}10 \times 10^5 \text{ kg s}^{-1}$. On 15 April, a new crater opened up 0.5 km northwest of the initial main vent. The new vent gradually became the center of activity. This shift in activity

was accompanied by an initial drop in plume height and much reduced ash fallout. Vigorous explosive eruption activity picked up again and continued on 16 and 17 April. During 17 April, northerly winds carried the plume directly south. Ash clouds produced on 14–17 April spread to Western Europe, causing widespread closure of airspace. By 18 April, the vigor of the eruption had subsided significantly, marking the onset of the *second phase* (low-discharge effusive phase), which featured ~15 days of effusive activity with some weak explosive activity yielding minor tephra production. Lava emerged from the main vent on 21 April and advanced north along the path of the Gígjökull outlet glacier. During this period, the magma effusion rate mostly ranged from $0.1 \times 10^5 \text{ kg s}^{-1}$ to $1.1 \times 10^5 \text{ kg s}^{-1}$. Deep earthquakes detected in the first days of May signaled renewed injection of magma into the volcano plumbing system; at the same time, effusion of lava came to a halt. On 5 and 6 May, the vigor of the explosive activity intensified, signaling the onset of the *third phase* (second explosive phase), which produced 8- to 10-km-high eruption columns and ash plumes that again reached Europe. The magma eruption rate during the third phase is estimated at $3\text{--}10 \times 10^5 \text{ kg s}^{-1}$. The *final phase* began on 18 May, when the eruption intensity declined significantly and continued on that path until cessation of sustained eruption on 22 May, after 39 days of continuous activity. Minor explosions involving small amounts of magma took place on 4 to 8 June, and a single, small explosion occurred on 17 June. Steam emission continued for months following the eruption.

3. The Volcano Sensor Web

[11] Having described the phases of the 2010 eruption, we now examine the assets used to observe it remotely under the auspices of the VSW. The Volcano Sensor Web has fully automated the process of retasking a spacecraft (EO-1) to obtain observations of volcanic eruptions [Davies *et al.*, 2006a]. The spacecraft control system is triggered by detections of ongoing volcanic activity from other sources (Table 1), some of which are automated themselves. Triggers leading to requests for EO-1 observations fall into three categories; (a) spacecraft-based, (b) in situ, and (c) other observational triggers. Originally envisioned as a test bed to demonstrate autonomous spacecraft and sensor web applications for planetary exploration [Chien *et al.*, 2006], the streamlined spacecraft command and control and resource allocation system has proved highly valuable for observing dynamic processes on Earth, including volcanic eruptions, earthquake damage, flooding (e.g., Mississippi River, 2011), wildfires [Chien *et al.*, 2011], and tsunami damage (Sumatra, 2004; Tohoku earthquake, 2011). EO-1 can now be retasked with a few key-strokes, a process that in 2003 took approximately 3 weeks.

[12] Since its inception, the VSW has grown to include triggers from a broad range of resources. Between May 2004 and February 2011, the VSW/Autonomous Spacecraft yielded 3656 EO-1 observations of volcanoes around the world. Volcanoes and number of observations per volcano are shown in Figure 2. VSW volcanic activity triggers and subsequent data flow are illustrated in Figure 3.

[13] The VSW has supplied data at short notice in sometimes critical situations where remote-sensing data provided

Table 1. Volcano Sensor Web Trigger Mechanisms 2004–2012

Data source	Asset Name/Location	Data Source	VSW Trigger	Coverage	Operational History	References	Notes
1. Spacecraft data processing application	EO-1—ASE (Autonomous Sciencecraft)	Hypertion spectrometer	Detection of hot pixels	Global	2004–	[Chien <i>et al.</i> , 2005b; Davies <i>et al.</i> , 2006a]	Demonstration of autonomous science-driven spacecraft operations
	MODVOLC (University of Hawai'i)	Earth-orbiting MODIS instruments	Detection of hot pixels	Global	On-line since 2005	[Wright <i>et al.</i> , 2002; Wright <i>et al.</i> , 2004]	MODIS is on the NASA <i>Terra</i> and <i>Aqua</i> spacecraft
	GOESVole (University of Hawai'i)	Platforms in geostationary orbit	Detection of hot pixels	Primarily Hawai'i; Pacific rim volcanoes	Online 2005–2006	[Davies <i>et al.</i> , 2006b; Harris <i>et al.</i> , 1997; Harris and Thornber, 1999]	GOES spacecraft in geostationary orbit, observing Pacific and Pacific rim
2. In situ instrumentation	Mount Erebus Volcano Observatory	Acoustic sensors	Strombolian event detection	Mount Erebus, Antarctica	2004–2007	[Aster <i>et al.</i> , 2004; Davies <i>et al.</i> , 2006a]	Erebus Volcano Observatory is operated by New Mexico Tech, Socorro, NM
	USGS Hawaiian Volcano Observatory (Hawai'i)	VALVE—tiltmeter network	Tilt behavior indicative of impending eruption	Kilauea, HI	2005–2006	[Cervelli and Miklius, 2003]	VALVE incorporates tilt, seismic, and gas data and automatically issues alerts
3. Ash advisory	USGS HVO/NPS-HVNP (Hawai'i)	Volcano Monitors (VM)	Anomalous SO ₂ detection	Kilauea, HI	2006–2008	[Boudreau <i>et al.</i> , 2007; Davies <i>et al.</i> , 2008c]	Demonstrated EO-1-VM two-way triggering via VSW
	USGS Cascades Volcano Observatory (Vancouver, WA)	Volcano-monitoring deployable stations. “Spiders” (seismic, acoustic, gps)	Seismic alert	Mt. St. Helens, WA	2010–	[LaHusen <i>et al.</i> , 2010; Chien <i>et al.</i> , 2010a]	Fastest trigger-observation response obtained so far: 2 h (3 July 2005) from CVO seismic event detection
	Iceland Meteorological Office	Seismic, tilt, meltwater flow metering	Seismic alert	Iceland volcanoes	2010–	This paper	Grimsvötn 2011 eruption (see section B).
	Volcanic Ash Advisory Center (VAAC) alerts (seven centers)	Multiple (e.g., pilot reports)	Plume detection	Global	2005–	[Davies <i>et al.</i> , 2006b]	Many alerts worldwide, inc. Talang, 2005; Nyamuragira, 2006
4. Other reports of eruptions	US Air Force Weather Agency (AFWA) alert	Multiple (e.g., pilot reports)	Plume detection	Global	2005–		Multiple detections and triggers
	Multiple notification sources	Alert of impending or ongoing activity from media or colleagues	Manual	Global	2004–		Numerous events around the world, inc. Afar eruptions (Ethiopia/Eritrea), 2006–2011; Puyehue Cordon Caulle (Chile), 2011–2012

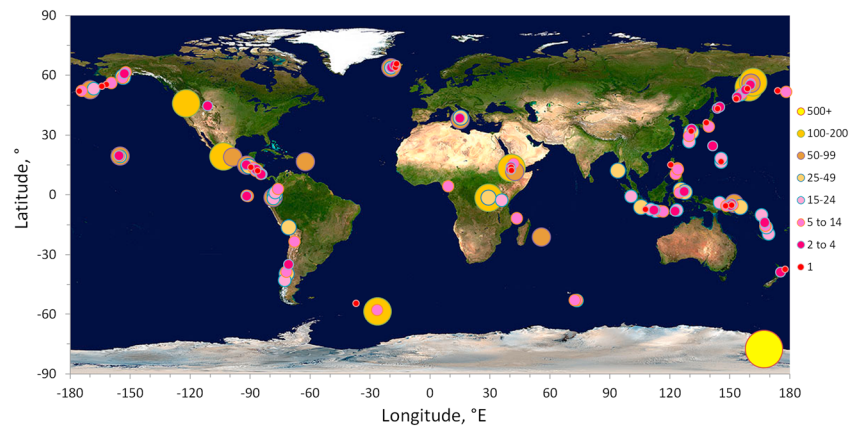
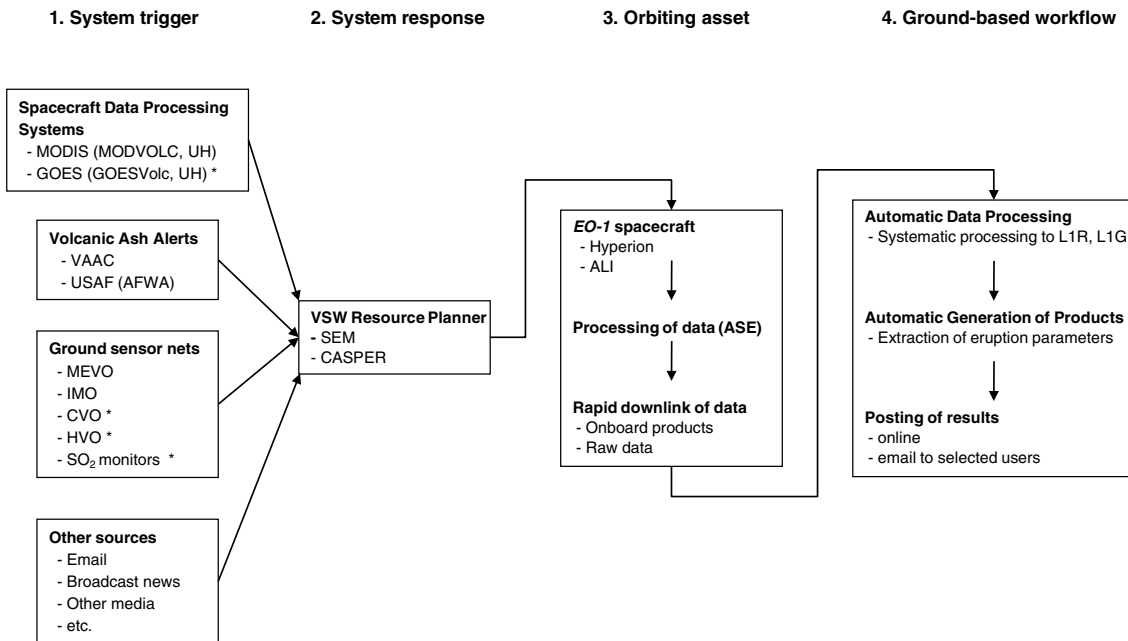


Figure 2. Observations of volcanoes obtained by *EO-1* from May 2004 to February 2011. The most observations (550) were obtained of Erebus volcano, Ross Island, Antarctica. The high latitude of Erebus coupled with the high inclination of *EO-1*'s orbit means that there are many more opportunities to image this volcano than for targets close to the equator [Davies *et al.*, 2008a]. Other frequently observed volcanoes include Mount St. Helens, U.S. (171 observations); Erta'Ale, Ethiopia (75 observations); and Etna, Italy (75 observations). Fifty observations of Fimmvörðuháls and Eyjafjallajökull were obtained between March and June 2010.



* Triggering from this source not currently active

Figure 3. Data flow through the Volcano Sensor Web. Individual components are described in the text. The left-hand portion of the figure deals with system triggers. VSW triggers come from a variety of sources, including applications processing spacecraft data and volcanic ash alerts. The resource management system processes the alerts, prioritizes targets, and inserts observations into the *EO-1* operational timeline. Data thus obtained can be processed onboard *EO-1*, but all data are now downlinked and processed on the ground as described in the text. Products are posted on a website and alerts e-mailed to interested parties. The entire process is autonomous. Successful detection of volcanic activity can be used to trigger requests for additional observations via the Science Event Manager (SEM) and Continuous Activity Scheduling Planning Execution and Replanning (CASPER) application. Key: UH=University of Hawai'i (Honolulu, HI); CVO=Cascades Volcano Observatory (Mt. St. Helens volcano); HVO=Hawai'i Volcano Observatory (Volcano, HI); MEVO=Mount Erebus Volcano Observatory (New Mexico Tech., Socorro, NM); IMO=Icelandic Meteorological Office; VAAC=Volcanic Ash Advisory Centers; USAF (United States Air Force) AFWA (Air Force Weather Advisory); *EO-1*=*Earth Observing 1*; ASE=Autonomous Sciencecraft software (on *EO-1*); ALI=Advanced Land Imager (on *EO-1*). The SO₂ monitors were small, self-contained units placed on Kilauea volcano, HI, to demonstrate autonomous, two-way sensor/spacecraft triggering [Boudreau *et al.*, 2007]. After Davies *et al.* [2006b].

the only means of assessing volcanic risk and hazard. The best example of this was during the eruption of Nyamuragira volcano, Democratic Republic of Congo, in November 2006, described in *Davies et al.* [2008b].

[14] The streamlining of *EO-1* operations resulting from implementation of ASE and VSW software meant that when Eyjafjallajökull erupted it was possible to quickly retask the spacecraft. A sequence of *EO-1* observations at unprecedented temporal resolution was obtained over the duration of the eruption. We report on the analysis of these observations in this paper.

4. *EO-1* and Spacecraft Autonomy

[15] Before describing the observations of the Eyjafjallajökull eruption, we now briefly describe the orbiting asset of the VSW, the *EO-1* spacecraft, and the instruments and software onboard.

4.1. *EO-1* Spacecraft

[16] The NASA New Millennium Program's *EO-1* was launched on 21 November 2000 into a highly inclined (98.2°), sun-synchronous, circular orbit at an altitude of 705 km. Target repeat time for daytime nadir observations is 16 days. The ability to point the spacecraft across-track

allows targets to be imaged from adjacent tracks to the east and west [*Davies et al.*, 2008a]. If the number of accessible adjacent tracks to the east and west is two, then this enables up to 10 observations of a target every 16 days (five during the day on descending tracks and five at night on ascending tracks). For high-latitude targets (above $\approx 70^\circ$), the number of adjacent tracks from which a target can be imaged increases markedly [*Davies et al.*, 2008a]. Onboard *EO-1* are two imagers, Hyperion and ALI, and the Autonomous Sciencecraft software (ASE) [*Chien et al.*, 2005b; *Davies et al.*, 2006a; *Doggett et al.*, 2006; *Ip et al.*, 2006].

4.2. Hyperion Hyperspectral Imager

[17] The hyperspectral Hyperion imaging spectrometer on *EO-1* is described by *Pearlman et al.* [2003]. Hyperion has 220 discrete usable bands covering 0.4 to $2.5\ \mu\text{m}$ with a spectral resolution of 10 nm. This spectral range makes Hyperion an ideal instrument for detecting the heat from the hottest areas ($>500\ \text{K}$) of ongoing volcanic activity [*Davies et al.*, 2006a]. A Hyperion observation swath is 7.7 km (256 pixels at 30 m/pixel) wide and can be up to 185 km long. Examples are shown in Figure 4 (details of the physical volcanic eruptions seen here are given below). Radiometric correction of Hyperion data is described by *Beck* [2003].

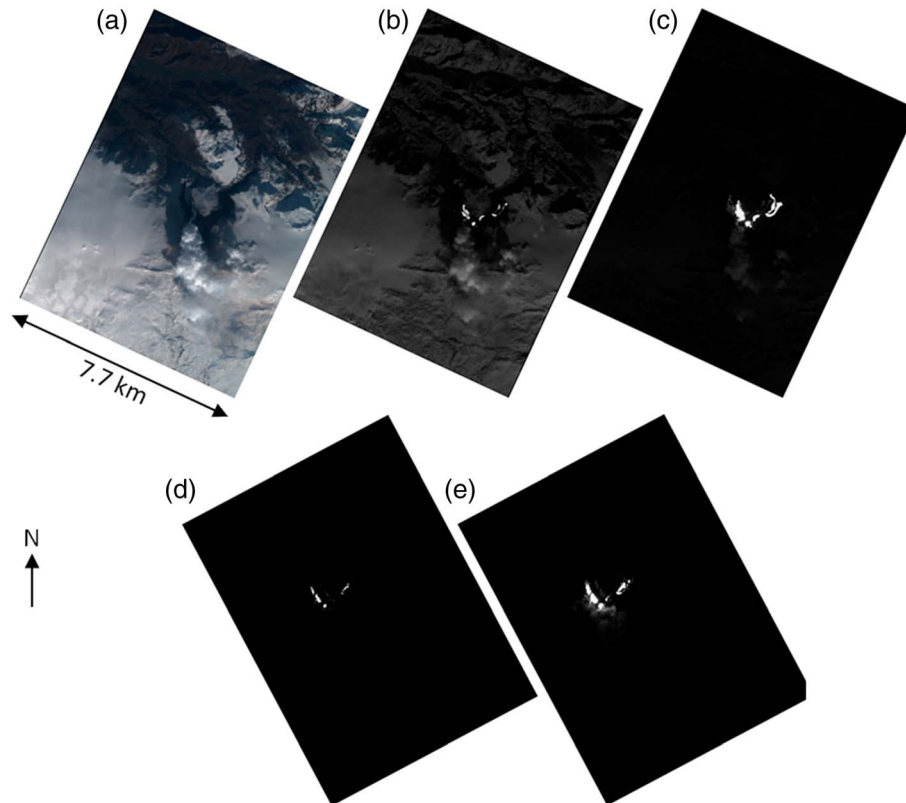


Figure 4. Hyperion data obtained on 1 April 2010 of the eruption at Fimmvörðuháls. (a–c) Data obtained during the day (11:52.38 UT) and (d–e) data obtained the following night (21:30:12 UT). Figure 4a is constructed from visible wavelength data, using band 28 ($0.630\ \mu\text{m}$) for the red channel, band 20 ($0.549\ \mu\text{m}$) for the green channel, and band 13 ($0.478\ \mu\text{m}$) for the blue channel. Figure 4b shows band 110 ($1.245\ \mu\text{m}$), where the location of the hottest lava surfaces become apparent. Figure 4c, band 210 ($2.254\ \mu\text{m}$), reveals the complex distribution of hot pixels resulting from a mixture of lava fountaining from the active vents and open channel flow in the lava flow field. See also Figure 7. Figure 4d is band 110 ($1.245\ \mu\text{m}$). Figure 4e is band 210 ($2.254\ \mu\text{m}$).

4.3. ALI (Advanced Land Imager)

[18] The EO-1 ALI is a multispectral instrument with 10 bands covering 0.4 to 2.4 μm . The PAN (panchromatic) band covers 0.48–0.69 μm at a resolution of 10 m/pixel. The other nine bands cover the visible and near-infrared to the SWIR with data at a spatial resolution of 30 m/pixel. ALI data are collected in four swaths covering an area 37 km wide and 42 to 185 km in length. An example of part of an ALI observation is shown in Figures 5 and 6. ALI provides a wider image than Hyperion, so ALI data are especially useful for examining larger-scale eruption products (such as the extent of ash deposits) and for estimating the heights of volcanic plumes in observations where the highest part of the plume and its shadow can be seen [Glaze *et al.*, 1999].

4.4. Autonomous Sciencecraft (ASE) Software

[19] ASE is software that allows autonomous spacecraft command and control, resource management, and onboard analysis of Hyperion data to detect a wide range of ongoing dynamic processes. ASE is described in detail elsewhere [Chien *et al.*, 2005b; Davies *et al.*, 2006a; Doggett *et al.*, 2006; Ip *et al.*, 2006]. For the purpose of monitoring volcanic activity, ASE includes a Hyperion data onboard processing

capability to flag anomalous high-temperature ($>460\text{ K}$) areas using an algorithm called THERMAL_CLASSIFIER [Davies *et al.*, 2006a]. From 2004 until 2008, data of only these thermally active areas were preferentially and rapidly returned to the ground for additional autonomous processing, often within 30 min after acquisition, and ASE could retask EO-1 to obtain further observations. Recent improvements in data transmission mean that now the full Hyperion data sets are autonomously processed with THERMAL_CLASSIFIER on the ground typically within 2–4 h of acquisition, although the onboard capability still remains.

5. Hyperion Data Analysis

[20] Hyperion high-temperature volcanic thermal emission data are fitted with a “one size fits all” work flow. Raw Hyperion radiance data (level L0 data) are first radiometrically corrected (see description in Doggett *et al.* [2006]). Corrections to radiance are made for spacecraft viewing angle and distance to target. The Hyperion data-processing chain processes all of the raw Hyperion data to Level 1R (radiometrically corrected radiance). Areas identified by the THERMAL_CLASSIFIER [Davies *et al.*, 2006a] are flagged for additional processing.

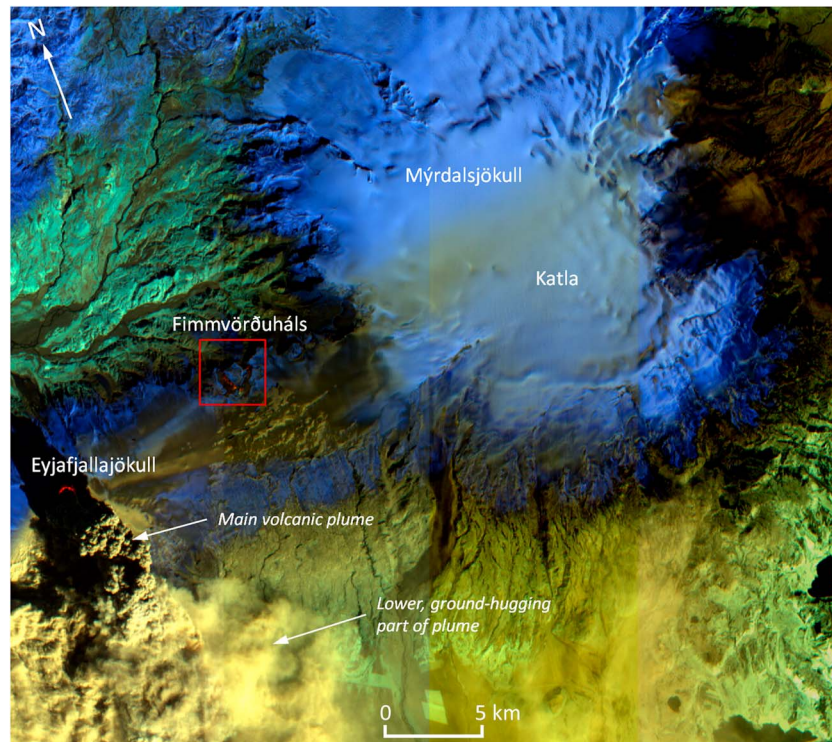


Figure 5. ALI observation EO1A2190152010107110KF obtained 17 April 2010. This short-wavelength false-color infrared image shows the Eyjafjallajökull eruption on the left, with a plume heavily laden with ash. This event caused major travel problems, closing most European airspace. Also labeled is the ground-hugging portion of the plume. This image was created from ALI bands MS-7 (2.08–2.35 μm) (used as the red channel in this RGB image), MS-5 (1.55–1.75 μm) (green channel), and MS-5' (1.2–1.3 μm) (blue channel). Spatial resolution is 30 m/pixel. The hottest pixels appear red. Snow and ice appear blue. An intense thermal source is visible at the base of the plume in the cauldron that has formed in the icecap. To the ENE is the Fimmvörðuháls lava flow field (within the red box), which had stopped flowing by this time but was still hot (Figure 6 shows these flows in more detail). Further to the east is Mýrdalsjökull, under which is found the volcano Katla. The image is 37 km wide.

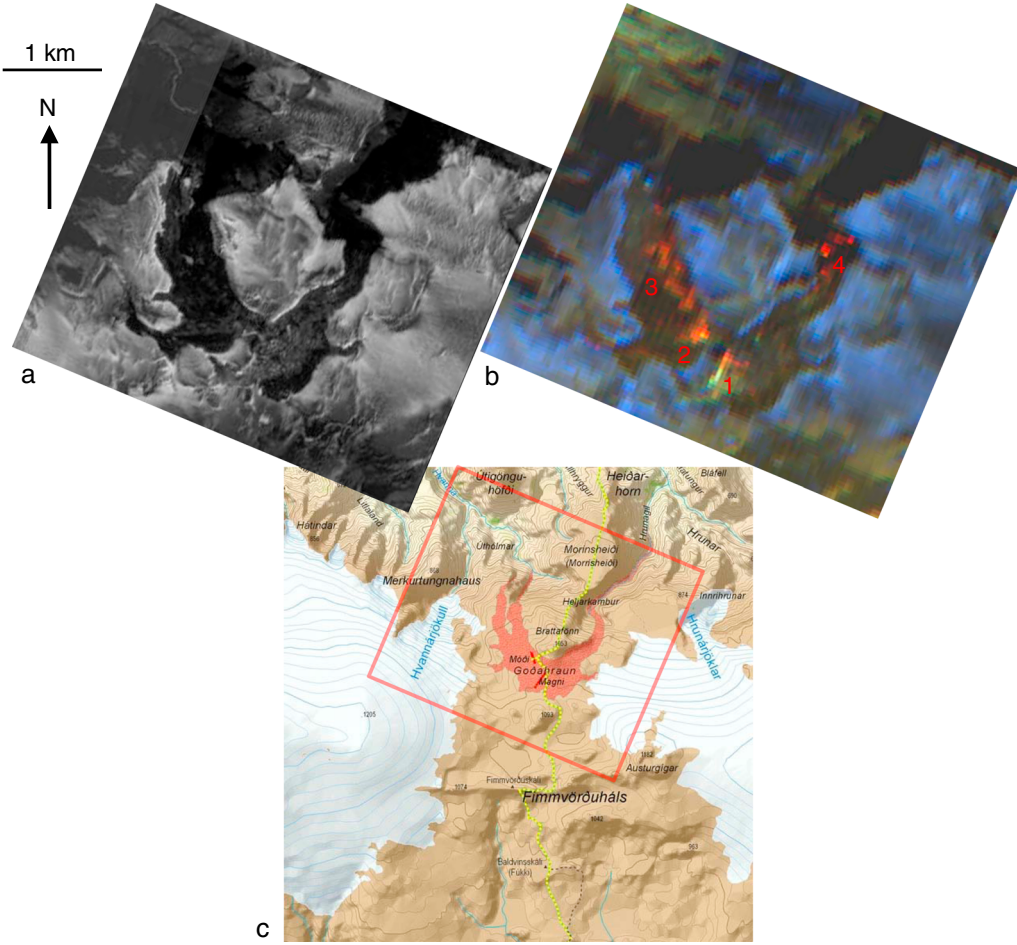


Figure 6. Fimmvörðuháls flows as seen in ALI observation EO1A2190152010107110KF, obtained 17 April 2010. (a) Detail of ALI PAN band (0.48–0.69 μm), showing the lava flows (dark surfaces) emplaced between 22 March 2010 and 12 April 2010. PAN data are at 10 m/pixel. (b) SWIR data at 30 m/pixel (see Figure 5), showing the location of the hottest surfaces (red/orange/yellow pixels). The hot pixels at 1 and 2 are the locations of the main vents. Location 2 covers the two main vents that produced most of the lava along the NW fissure that fed the flows (location 3). Location 4 denotes the top of a steep slope over which lava flowed, into Hrunagil, earlier in the eruption. Even though the eruption stopped on 12 April 2010, the lava flows still have partially molten interiors at very high temperatures (>1200 K). (c) Context map on which the Fimmvörðuháls lava flows are shown in pink. The location of the two eruption fissures are shown as red lines. The red box shows the area covered by Figures 6a and 6b.

[21] The data processing methodology is described in detail in *Davies et al.* [2008a]. In summary, radiant flux at each usable Hyperion wavelength (data at wavelengths where the detector is saturated are discarded) from each thermally active pixel is corrected for atmospheric absorption and reflected sunlight (daytime observations only); the radiance data are fitted with a best-fit, single-temperature blackbody model yielding a color temperature; and the (typically) sub-pixel area at this temperature is calculated. We note that a desirable future refinement would be to use a model utilizing a combination of two to seven blackbody curves [*Wright et al.*, 2010] to yield a more accurate estimate of temperature distribution and thermal emission.

[22] Having determined temperature and pixel fraction for each hot pixel, the total thermal emission from the active parts of the flow (Q_{TOT} , that is, the sum of radiant flux Q_{rad} and convective heat loss Q_{conv}) is calculated for the observation as a whole. The total heat loss is converted to an

estimate of minimum effusion rate (Q_F , $\text{m}^3 \text{s}^{-1}$) [*Harris et al.*, 1999; *Harris and Thornber*, 1999] where

$$Q_F = \frac{Q_{\text{TOT}}}{\rho_{\text{lava}}(c_p \Delta T + L \Delta f)} \quad (1)$$

[23] The automatic system uses the thermo-physical properties of basalt to calculate Q_{rad} , Q_{conv} , and Q_F where $\rho_{\text{lava}} =$ lava density (2600 kg/m^3 , close to the actual value for basalt of 2800 kg/m^3 and the value of 2500 kg/m^3 for benmoreite), $\Delta T =$ temperature range through which the lava has cooled (200 K), $L =$ latent heat of fusion ($3 \times 10^5 \text{ J/kg}$), $c_p =$ lava specific heat capacity (1150 J/kg/K), and $\Delta f =$ change in crystallization fraction over ΔT (0.45).

5.1. Data Products

[24] Automatic Hyperion data processing yields the products listed in Appendix A. All of the data and products are posted on a website for rapid access and examination.

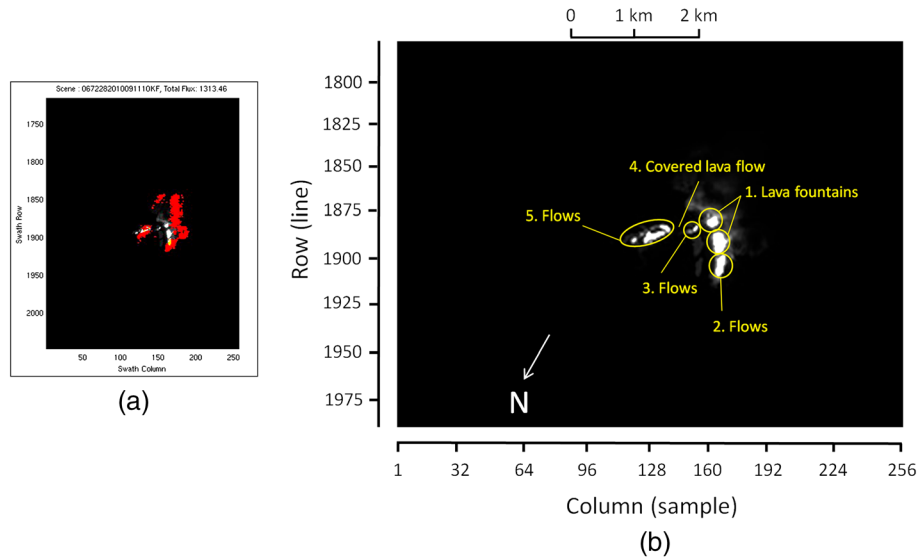


Figure 7. Examples of products automatically generated by the VSW from a Hyperion observation (EO1H0672282010091110KF) of the Fimmvörðuháls eruption obtained on the night of 1 April 2010 at 21:30 UT. (a) Map identifying thermally anomalous pixels (red) and the most intense pixels in white and yellow as detected using the THERMAL_CLASSIFIER algorithm. (b) The observation at 2.285 μm (band 213), with eruption style identified by observers on the ground. The identification of eruption style will allow more informed analysis of the Hyperion data.

[25] Examples of some of the automatically generated products are shown in Figures 7 to 10. Figure 7a shows a map of pixels with anomalous thermal emission, as detected by the ASE THERMAL_CLASSIFIER in a nighttime observation of the Fimmvörðuháls flow field obtained on 1 April 2010 (see also Figure 4d). The pixels with the highest radiance are coded yellow and white. The red pixels are lower-temperature detections that are mostly a diffused glow within the plume. Figure 7b shows the hottest parts of Figure 7a where various components of the ongoing activity are labeled in accordance with on-site observations made by two of the authors (T.T. and A.H.) in the daytime on 1 and 2 April. The two lava fountaining vents are feeding lava to the active flow fronts via open channel flow. The thermal continuity of the channel feeding the northeast branch of the flow field is disrupted, most likely by the presence of a thick and cool cover of surface rubble.

[26] Table 2 shows the VSW-generated eruption parameters that are created for each observation where ongoing volcanic thermal emission is detected. The effusion rate generated by the automatic system is probably a substantial underestimate. As noted above, the system, by necessity, uses a “one size fits all” approach for all erupting volcanoes regardless of style of eruption.

[27] The Eyjafjallajökull eruption is particularly valuable because the eruption was studied in great detail, including estimation of effusion rate on almost a daily time frame [Gudmundsson *et al.*, 2012]. This allows the comparison of effusion rates derived from Hyperion data with those derived on the ground (from in situ measurements of flow coverage rate and thickness or from the height of the eruption column [Gudmundsson *et al.*, 2012]). Quantifying the magnitude of the underestimation of Hyperion-derived effusion rate is a useful parameter in interpreting data from eruptions where there are no ground-truth data against which remote-sensing data can be compared.

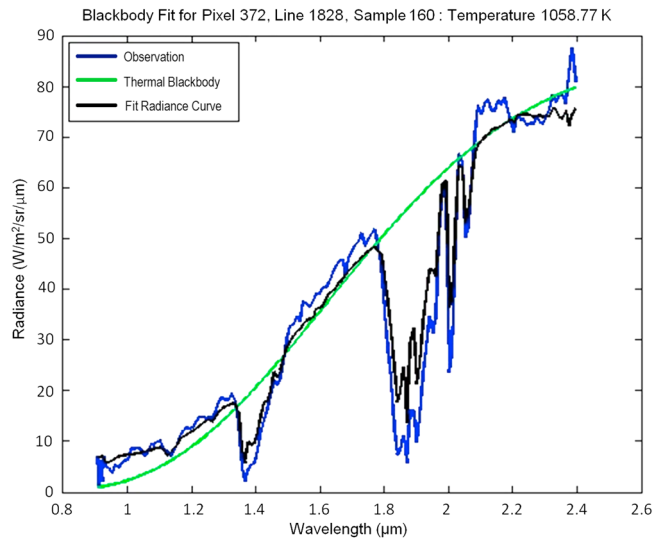


Figure 8. Example of VSW fit to Hyperion data. This is the spectrum of the pixel at sample 160, line 1828 of Fimmvörðuháls observation EO1H2180152010091110PF. The daytime observation was obtained on 1 April 2010 at 11:52 UT. The pixel covers part of an active lava flow. None of these data are saturated. The data (blue line) have been radiometrically corrected, corrected for incident sunlight, further corrected for emission angle and range to target (black line), and then fitted iteratively with a Planck black body function (green line) to determine the best-fit temperature of the thermal source, as well as the pixel fraction occupied by that source. The best-fit temperature is 1059 K, and the area is 14 m^2 . Total radiant power is 1 MW.

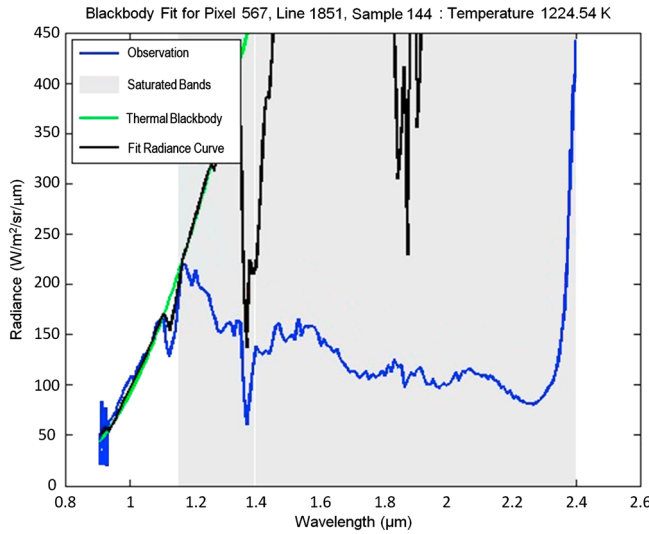


Figure 9. Example of extreme saturation of Hyperion data. Hyperion radiance spectrum of a pixel containing a lava fountain (identified as such by observers on the ground). Intense thermal emission has saturated the Hyperion detector at wavelengths greater than $1.16 \mu\text{m}$. These saturated wavelengths are within the area shaded gray. The “dip” at $2.3 \mu\text{m}$ in the “observation” spectrum (blue line) is a characteristic of saturation [see Davies *et al.*, 2006a]. The pixel location is sample 144, line 1851 of observation EO1H2180152010091110PF, a daytime observation of Fimmvörðuháls obtained on 1 April 2010. The unsaturated data at wavelengths from $0.9 \mu\text{m}$ to $1.16 \mu\text{m}$ are sufficient to allow determination of a best-fit temperature of 1225 K. The area at this high temperature is 0.097 of 900 m^2 , or 87 m^2 , equivalent to a circular area $\sim 11 \text{ m}$ in diameter. Radiant power from this pixel alone is therefore 11 MW.

[28] Figure 8 shows an example of a single-temperature fit to a Hyperion spectrum. The fit is to data that have been corrected for emission angle, incident sunlight, and atmospheric absorption. Such images are created for every pixel that triggers the THERMAL_CLASSIFIER (see Figure 7a).

[29] Figure 9 shows an extreme case, where the intensity of thermal emission has saturated the Hyperion detectors at most wavelengths. One particular strength of the Hyperion data and the algorithm we use to fit the data is that despite the loss of most wavelengths there are always some wavelengths at the short end of the Hyperion wavelength table that are unsaturated. These remaining wavelengths are used to derive a temperature, the pixel fraction occupied by the emitting surface, and finally the contribution of this thermal source to overall power output.

[30] Figure 10 shows histograms of the number of pixels at a given temperature for the data identified in the day and night observations of Fimmvörðuháls on 1 April 2010. Activity changed markedly between the two observations (about 12 h), with a narrower range of temperatures seen during the night. This change in level of activity follows what was seen by observers on the ground. The total thermal emission detected in these two observations was 1.77 GW in the daytime observation and 0.4 GW in the nighttime observation, a significant reduction in activity in the space of 12 h. It may be that at the time of the nighttime observation lava fountaining had decreased, and, therefore, detectable areas

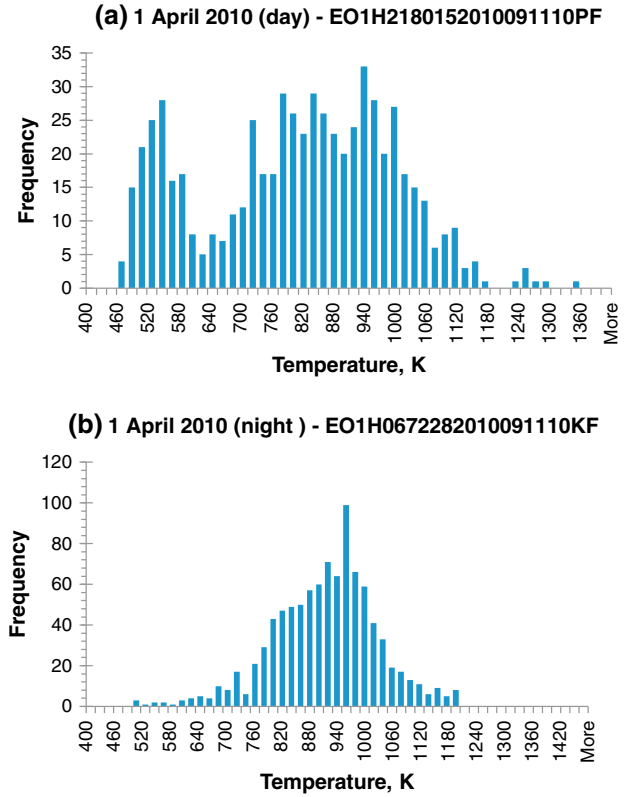


Figure 10. Histograms of derived temperatures for day and night Hyperion observations obtained on 1 April 2010, revealing the complex distribution of surface temperatures even with single-temperature fits to the Hyperion spectra. There is also significant change in the temperature distributions from the daytime observation (which exhibits a dual peak) to the nighttime observation some 12 h later (a more Gaussian distribution).

Table 2. Eruption Parameters Generated by the VSW Hyperion Data Processing System for the Observation in Figure 7

Parameter or Quantity	Value	Units
Mass effusion rate	1314	kg s^{-1}
Volumetric effusion rate, (Q_F)	0.53	$\text{m}^3 \text{s}^{-1}$
Total power loss, (Q_{TOT})	3.94×10^8	W
Radiant power loss, (Q_{rad})	3.37×10^8	W
Convective power loss, (Q_{conv})	5.75×10^7	W
Total effective area	1.05×10^4	m^2
Effective temperature	867	K
Look angle	11.35	°
Range to ground	705.38	km

at the highest temperatures seen in the daytime observation were not present or were too small to be detected in the nighttime observation.

[31] In addition to the products described above, the L1R Hyperion and ALI data are processed to generate a geolocated product (L1G) that includes terrain correction using a digital elevation model (DEM) to correct parallax error due to topographic relief. Whereas these reprojected data are not suitable for quantitative analysis of thermal emission due to resampling of the data, they provide a more accurate location of features.

[32] All products are generated and posted within a few hours of observation acquisition by *EO-1*. Actual posting time is dependent on spacecraft downlink timing. The facility exists for some of the products automatically generated by VSW processing workflow to be posted automatically to members on a preexisting e-mail list.

6. *EO-1* Observations of Eyjafjallajökull Volcano, 2010

[33] As described above, the 2010 eruption of Eyjafjallajökull began on 20 March 2010 in Fimmvörðuháls, the mountain pass between Eyjafjallajökull and Mýrdalsjökull. With no link between in situ sensors and the VSW, there was no automatic triggering of the sensor web. Instead, commercial news reports alerted the VSW team to the ongoing eruption, and, with the onset of the eruption taking place at a weekend, retasking *EO-1* took longer than it would have if the triggering had been alerted autonomously. Subsequently, of course, alerts poured into the VSW from space-based assets (MODVOLC, at the University of Hawai'i, which processes MODIS data) and from the London Volcanic Ash Advisory Center (VAAC). The first *EO-1* observation of the eruption at Fimmvörðuháls was therefore obtained on 24 March 2010. This image showed lava fountains and multiple lava flows, one of which flowed north.

[34] Data products generated by the automatic system were transmitted to volcanologists in Iceland. Between 24 March and 5 June 2010, 50 observation pairs (each pair consisting of a Hyperion and ALI observation) were obtained by *EO-1* of this eruption. About 50% of these observations were of limited use due to cloud cover masking the eruption site.

[35] The following section describes the timeline of activity as seen by *EO-1*, annotated with notes from observers watching the eruption from nearby. *EO-1* observations obtained are detailed in Table 3.

6.1. Fimmvörðuháls Eruption: 20 March 2010 to 12 April 2010.

[36] *24 March 2010*. The first observations by Hyperion and ALI were obtained on 24 March 2011 (Figure 11) and showed intense thermal emission from lava fountains and lava flows. Figure 11 shows part of the ALI PAN image (spatial resolution 10 m/pixel) and the contemporaneous Hyperion SWIR image (resolution 30 m/pixel). Observers on the ground watched as lava erupted from vents along a SW-NE trending fissure and flowed northeastward into a gorge named Hrunagil. A lava channel approximately 30 m wide can be seen in the PAN data (Figure 11a). The extreme thermal emission from lava tumbling over a cliff and down a steep slope into Hrunagil can be seen in the Hyperion SWIR data and even in the shorter-wavelength ALI PAN data. From the Hyperion data, the energy loss (~80% radiative and ~20% convective) from the lava flows was 2 GW, with some modeled temperatures exceeding 1220 K. This thermal emission yielded an estimate of ~3 m³ of lava erupting every second. This estimate of effusion rate is an underestimate, as it does not take into account flow inflation (which is not detectable from measurements of thermal emission) and emission from cooler surfaces that are not detected by the THERMAL_CLASSIFIER algorithm. A plume is seen

emanating from the vent. Another white plume (indicating the plume is mostly water vapor), originating from a point source in Hrunagil, is created by the interaction of incandescent lava and water generated by melting of the surface snow cover.

[37] *29 March 2010*. Through a thin cloud layer, Hyperion data showed intense thermal emission from the vent region and varying thermal emission along the length of lava flowing to the northeast and into Hrunagil. Total power loss of 6 GW was estimated from the Hyperion data, the highest thermal output seen by Hyperion during the entire eruption (Table 3). On the ground, observers noted a distinct pulsation in the vigor of the eruption [Thordarson *et al.*, 2011].

[38] *30 March 2010*. A nighttime observation showed two bright thermal sources within 100 m of each other and fainter thermal emission from hot surfaces almost surrounding the hill to the north of the first fissure.

[39] *1 April 2010*. The day before (31 March 2010), a second eruptive vent had opened up just north of the first fissure. Day and nighttime observations were obtained on 1 April 2010 under perfect viewing conditions. Hyperion observations are shown in Figure 4 and Figure 7. VSW processing of the Hyperion data yields the eruption parameters in Table 2. Thermal emission was from lava fountains emerging from the vents on the original fissure as well as the more strongly fountaining vents on the new NW-trending fissure. Lava emerged from both vents via open channels. A power loss of 1.8 GW was estimated from the nighttime observation.

[40] *4 April 2010*. A daytime Hyperion observation showed intense thermal emission from a new fissure and lava flowing to the northwest into a gorge named Hvannárgil, as well as fainter thermal emission from vents along the old fissure and the northeast flow. Temperatures as high as 1360 K were derived from the Hyperion data, remarkably high for single-temperature fits that tend to underestimate actual peak temperature present, with a total power output of 1.5 GW from an area of 0.046 km². Observers on the ground measured peak temperatures of 1287 K (1014 °C) at incandescent lava flow fronts. Temperatures within the vent were almost certainly higher, as suggested by Hyperion data.

[41] *6 April 2010*. A daytime Hyperion observation showed intense thermal emission from a vent on the new fissure and lava flowing into Hvannárgil. Lava interacting with meltwater generated a white plume.

[42] *7 April 2010*. A nighttime observation through a thin cloud layer showed a single vent and branching lava flows. Thermal emission was detected along segments of the flows. Observed power output dropped to 40 MW.

[43] *8–12 April 2010*. Bad weather prevented observations of Fimmvörðuháls. The eruption ended on April 12. During this eruption, lava covered ~1.3 km² with a thickness outside the crater rims reaching 30 m closest to the vents on the east side, but typically the thickness is 10–15 m, with an overall average flow thickness of 15.4 m [Edwards *et al.*, 2012].

6.2. Eyjafjallajökull: 14 April 2010 to 7 June 2010

[44] *14 April 2010*. *EO-1* was still tasked to observe Fimmvörðuháls when the eruption of Eyjafjallajökull began early on 14 April 2010. A daytime Hyperion observation on 14 April 2010 saw part of the plume from Eyjafjallajökull. A subsequent nighttime observation of Fimmvörðuháls by

Table 3. EO-1 Observations of Fimmvörðuháls and Eyjafjallajökull, 24 March 2010–5 June 2010

Date, Time (UT) mm/dd/yy hh:mm	Q_{rad} GW	Q_{conv} GW	Q_{TOT} GW	Estimated Effusion Rate, Q_F $\text{m}^3 \text{s}^{-1}$	Equivalent Mass Flux 10^3kg s^{-1}	Cloudy?	Eruption and Weather Notes
3/24/10 12:12	1.61	0.37	1.98	2.6	6.6	no	Eruption had started on 20 Mar. Lava fountains and flow seen.
3/29/10 12:06	5.40	0.55	5.95	7.92	19.8	partially	Intense thermal source at origin to SW. Lava flow to NE.
3/30/10 22:22	0.11	0.03	0.14	0.19	0.5	possibly clear	Two thermal sources—possibly a lava flow surrounding the mound.
4/1/10 12:22	1.46	0.30	1.77	2.35	5.9	no	Multiple vents and flows (see Figure 4).
4/1/10 22:00	0.34	0.06	0.39	0.53	1.3	no	Lava fountains and flows (see Figures 4 and 7).
4/4/10 12:38	1.23	0.25	1.48	1.97	4.9	no	Multiple flows, vents.
4/6/10 12:16	0.24	0.10	0.34	0.45	1.1	yes	Two intense sources visible through cloud.
4/6/10 21:54	<0.01	<0.01	0.01	0.01	<0.1	yes	Very diffuse thermal signal.
4/7/10 22:32	0.03	<0.01	0.04	0.05	0.1	yes	Single very intense spot. Diffuse signal from flow.
4/8/10 11:54	1.33	0.29	1.62	2.16	5.4	no	Intense thermal emission from fountains, lava flows.
4/9/10 12:32	0	0	0	0	0	yes	Nothing seen.
4/9/10 22:10	0	0	0	0	0	yes	Extremely diffuse thermal signal, possibly through cloud.
4/12/10 22:26	0	0	0	0	0	maybe	Faint thermal source. Fimmvörðuháls episode ends.
End of Fimmvörðuháls eruption—12 April 2010							
4/14/10 12:26	0	0	0	0	0	yes	White plume from new Eyjafjallajökull eruption.
4/14/10 22:04	0	0	0	0	0	yes	No thermal emission from Fimmvörðuháls detected.
							Intense thermal emission from Eyjafjallajökull seen in ALI nighttime observation.
4/16/10 12:04	0	0	0	0	0	yes	White plume from Eyjafjallajökull eruption.
4/17/10 12:42	0.04	0.02	0.06	0.08	0.2	no	“Cauldron” image—dark ash plume.
4/17/10 22:20	0	0	0	0	0	no	Thermal emission possibly masked by plume.
4/19/10 21:58	0.02	0.01	0.03	0.04	0.1	yes	Strong hot spot seen through cloud.
4/22/10 12:36	<0.01	<0.01	<0.01	<0.01	<0.1	yes	Faint thermal source at base of plume.
4/22/10 22:14	0.07	0.02	0.08	0.11	0.3	no	Strong thermal source at base of plume.
4/24/10 12:14	0.07	0.03	0.10	0.13	0.3	no	Intense thermal source at base of plume.
4/29/10 12:08	0	0	0	0	0	yes	Top of relatively small white plume seen.
4/30/10 12:46	0.18	0.07	0.25	0.33	0.8	partially	Extended source to north of main vent. New lava channel forming.
4/30/10 22:23	0.03	0.01	0.04	0.05	0.1	maybe	Extended source—2 joined sources—vent and end of flow?
5/2/10 12:24	0.25	0.07	0.32	0.43	1.1	no	Extended source to north of main vent. New lava channel forming.
5/2/10 22:02	0.03	0.01	0.04	0.06	0.1	maybe	Impressive scene of plume lit from within.
5/4/10 12:02	1.27	0.37	1.64	2.18	5.5	no	Increase in activity—large ash plume—fine shot of lava in 2 km-long channel.
5/5/10 12:40	0.02	0.01	0.03	0.04	0.1	yes	Active vent visible through cloud.
5/5/10 22:17	0.19	0.04	0.23	0.31	0.1	no	Main vent and extended source/lava flow?
5/7/10 21:56	0.24	0.06	0.30	0.40	1.0	no	Intense source at base of plume.
5/8/10 22:33	0.43	0.11	0.54	0.72	1.8	no	Vent and head of lava flow—one of the clearest observations obtained.
5/12/10 12:12	0.67	0.13	0.80	1.06	2.7	yes	Intense hot spot seen through cloud—large dark plume imaged—a great ALI image.
5/13/10 12:50	0	0	0	0	0	yes	Top of dark plume seen—relatively small plume.
5/13/10 22:27	0	0	0	0	0	yes	Top of relatively small plume illuminated—a hint of diffuse thermal emission under clouds.
5/15/10 12:28	0.32	0.09	0.41	0.55	1.4	partially	Ash plume to SW—intense thermal source at main vent.
5/15/10 22:05	0.15	0.05	0.20	0.27	0.7	partially?	Vent observed—also small thermal sources to north (lava channel?).
5/17/10 12:06	0	0	0	0	0	yes	Top of dark ash plume seen—plume drifting east.
5/18/10 12:44	0	0	0	0	0	yes	Top of dark ash plume seen—plume drifting north.
5/20/10 21:59	0	0	0	0	0	partially?	Plume seen.
5/22/10 12:00	0	0	0	0	0	yes	Top of very small dark (ash rich?) plume visible.
5/23/10 22:15	0.03	0.01	0.04	0.06	0.1	maybe clear	No large plume seen.
5/25/10 21:53	<0.01	<0.01	<0.01	<0.01	<0.1	partially	One hot pixel detected—small plume.
5/26/10 12:54	0	0	0	0	0	no	Clear view of cauldron—small vapor cloud.
5/26/10 22:31	0	0	0	0	0	yes	Probably mostly cloud.
5/28/10 22:09	0	0	0	0	0	yes	Probably mostly cloud.
5/31/10 12:48	0	0	0	0	0	yes	
6/2/10 22:03	0	0	0	0	0	yes	Small plume.
6/4/10 12:04	0	0	0	0	0	yes	
6/5/10 22:19	<0.01	<0.01	<0.01	<0.01	<0.1	no (apparently)	Small plume (same as 2 June); small thermal source at base.

Non-bold = day observation

Bold = night observation

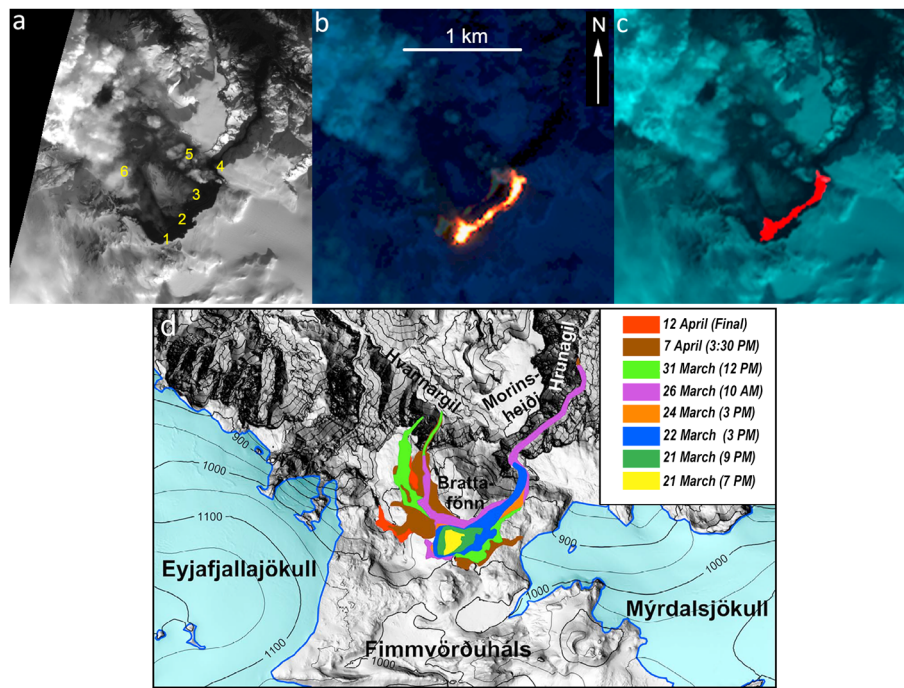


Figure 11. Observation of the Fimmvörðuháls eruption on 24 March 2010. This was the first observation of the eruption (which started 4 days earlier) by Hyperion and ALI on *EO-1*. (a) Part of the ALI PAN L1G image (spatial resolution 10 m/pixel) and (b) the contemporaneous Hyperion SWIR L1G image (resolution 30 m/pixel), created from Hyperion SWIR bands 213, 150, and 110 in the red, green, and blue channels, respectively. The intense thermal emission (red, yellow, and white pixels) comes from active vents along a SW-NE trending fissure and lava flows. (c) Overlay of Hyperion band 213 over two bands at visible wavelengths (28 and 20) to help locate the hot pixels with emplaced lava. Key to labeling in Figure 11a: 1 = location of main vent along the original fissure. 1 to 2 = fissure. 3 = lava flow channel within the flow field, ~30 m wide. There is a very bright pixel just southwest of the number “3” that is a high-temperature thermal source. 4 = bright thermal emission at head of Hrunagil (white patch). 5 = white plume from lava-meltwater interaction. 6 = plume from main vent. For comparison, (d) the lava flow emplacement sequence between 21 March and 12 April 2012 as derived by *Edwards et al.* [2012] (their Figure 2).

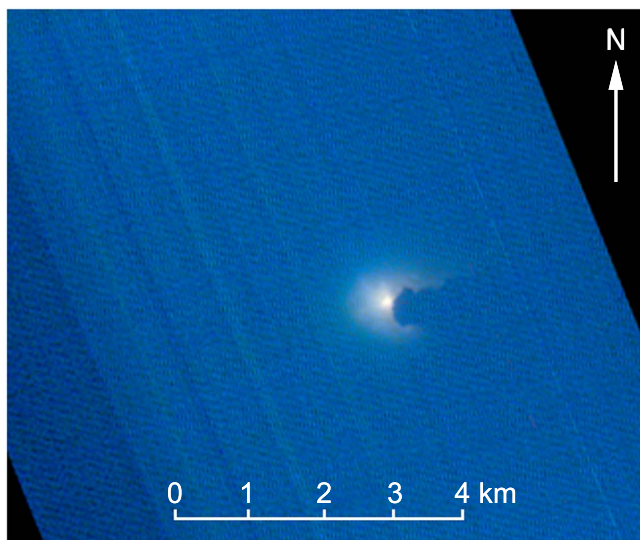


Figure 12. The first *EO-1* observation of Eyjafjallajökull which was obtained at night on 14 April 2010 at 22:26 UT by ALI. This image was created from three ALI SWIR bands. There is a low layer of cloud which is illuminated from below by an intense heat source. The cloud diffuses this energy, revealing the silhouette of the plume.

Hyperion did not detect any thermal emission (probably due to cloud), but the ALI nighttime observation detected a bright thermal emission source from Eyjafjallajökull in SWIR data. The thermal emission from the new vent was diffused by a layer of cloud. The silhouette of the plume, illuminated from below, is shown in Figure 12.

[45] 16–17 April 2010. The explosive eruption of Eyjafjallajökull continued, generating an ash plume that reached Northern and Western Europe and led to closure of airspace. In *EO-1* data, the ash plume was seen punching through a cloud layer on 16 April 2010. Cloud cover had gone by the next day, and a brown, ash-rich plume was observed on 17 April 2010 (see Figure 5), carried by winds to the south. An intense thermal source was seen by Hyperion in the cauldron, with a power output of at least 60 MW. Residual thermal emission from the Fimmvörðuháls lava flow field was also detected on 17 April 2010 (Figure 6).

[46] 19–24 April 2010. Numerous *EO-1* observations were obtained by day and night (Table 3). Thermal emission was often obscured by an ash plume (although much smaller than the massive ash plume of 17 April) and by cloud.

[47] 29–30 April 2010. Hyperion data hinted at an elongation in the thermal source toward the north. On-site and surveillance flight-based observations showed that after 21 April 2010 the lava emanating from the vents at the summit

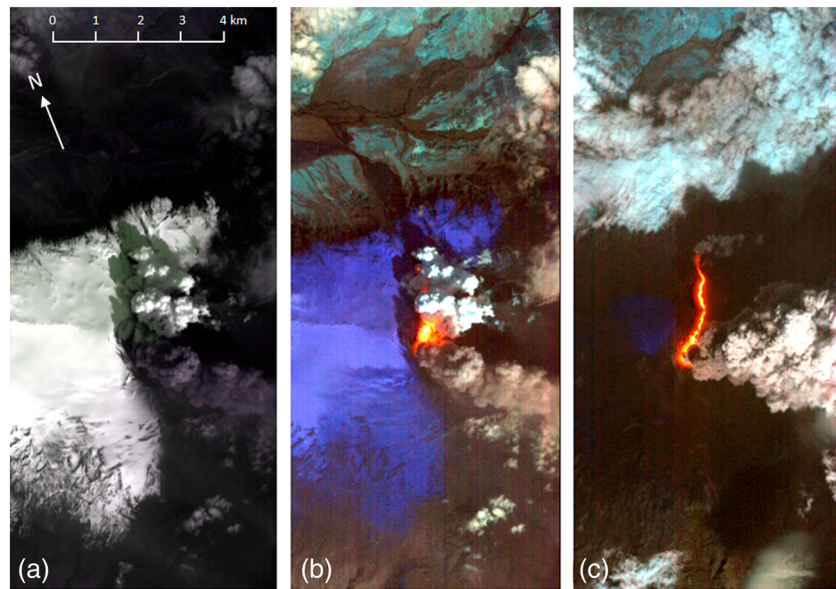


Figure 13. Eyjafjallajökull on 2 and 4 May 2010 as seen by Hyperion. (a) Visible wavelength Hyperion image at 30 m/pixel, showing a dark brown ash plume from the active summit vents and a white plume that is mostly water vapor created where lava is advancing northward down the path of and through the Gígjökull outlet glacier. (b) SWIR Hyperion image (created using bands 110 [1.242 μm], 150 [1.649 μm], and 213 [2.285 μm]) showing the hot (red and yellow) lava pixels in this lava flow, which is clearly revealed on (c) 4 May 2010, by which time the flow had advanced ~ 3 km from the source vent. Figure 13c uses the same bands as Figure 13b.

was working its way northward, initially beneath the ice but gradually melting the ice cover. This lava flow reached the northern margin of the summit caldera, about 1 km from the vent, and began to descend down the Gígjökull outlet glacier. From Hyperion data, observed power output was ~ 40 MW on the night of 30 April 2010.

[48] *1–7 May 2010.* In the first week of May 2010, Hyperion observed lava working its way down the path of the Gígjökull outlet glacier (Figure 13). Thermal emission estimates were generally low, compared with the peak of the Fimmvörðuháls eruption as estimated from Hyperion data. The eruption of more evolved and cooler magma with likely eruption temperatures in the range 1173 K to 1273 K (900–1000°C) may have contributed to this, but observations from aircraft indicated that the most likely explanation was that the initial advance of the lava occurred with much water-lava and ice-lava interaction. The formation of thicker insulating crusts than might have been expected led to lower lava surface temperatures. However, on 4 May 2010, a peak in activity occurred when minimum radiated power reached 1.3 GW. This peak was caused by a sharp increase in the magma discharge that resulted in an increase in the explosive activity, with a dark plume rising from the crater. These events were preceded by an elevated and upward-migrating swarm of volcano-tectonic earthquakes and reduced tremor. Poor weather impacted a Hyperion observation and also ground-based observations of ongoing activity.

[49] *12–26 May 2010.* A dark ash plume was seen by Hyperion on 12 May 2010, and the top of the ash plume was seen on 13 May 2010 in both day and night observations. A more or less steady dark ash plume was seen in day and night observations through 18 May 2010, and then

the level of volcanic activity dropped. A small diffuse plume was seen on 22 May 2010, no plume was seen on 23 May 2010, and on 26 May 2010 only steam was observed.

[50] *5–7 June 2010.* Hyperion detected ongoing activity in the form of two small thermal sources in nighttime observation on 5 June 2010 at the base of a small plume. Total power loss was estimated as ~ 2.3 MW. This was the last detection of thermal emission by EO-1 for the 2010 eruption.

7. Effusion Rate Estimation

[51] Figure 14 shows estimated effusion rate (kg/s) with time derived from Hyperion data, as well as estimated heat losses as measured by Hyperion and MODIS. Estimated effusion rates at Fimmvörðuháls, extrapolated from the rate of change of flow area at an observational temporal resolution of hours to several days, and effusion rate at Eyjafjallajökull from daily plume height measurements [Gudmundsson *et al.*, 2012] are shown in Figure 15.

7.1. Fimmvörðuháls: Effusion Rate From Hyperion Data

[52] Hyperion did not observe the first 3.5 days and last 2 days of the Fimmvörðuháls eruption. The estimated peak effusion rate from the Hyperion data was 1.7×10^9 kg/day ($\sim 8 \text{ m}^3/\text{s}$) on 29 March 2010 (see Table 3 and section 6). The variability of effusion rate is an indication of the dynamic nature of the eruption, with frequent lava-fountain episodes that contributed most of the thermal emission seen by Hyperion. Nevertheless, the trend in thermal emission is slightly downward until 4 April 2010. On 6 April 2010 there is a steep dip, probably mostly due to clouds obscuring thermal

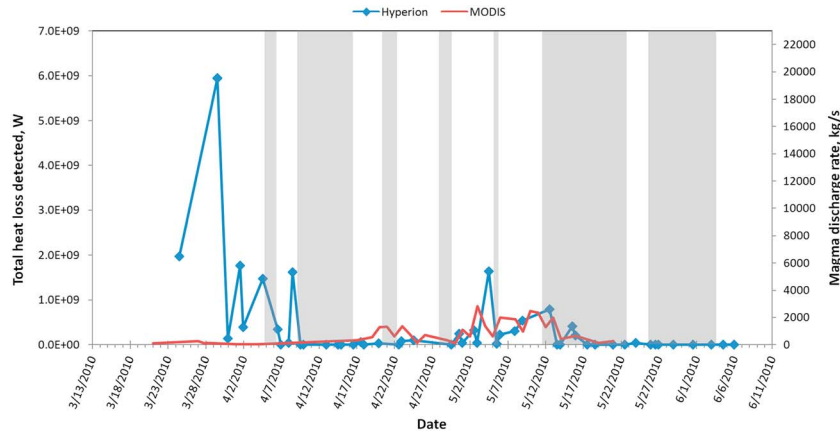


Figure 14. Variability of total heat loss (blue diamonds) detected by Hyperion for the Fimmvörðuháls and Eyjafjallajökull eruptions (see Table 3). Periods when observations were impacted by poor visibility are shown as gray areas. Also shown are estimates of thermal emission (red line) derived by MODIS instruments on the *Terra* and *Aqua* spacecraft, which fill some of the gaps in the Hyperion timeline.

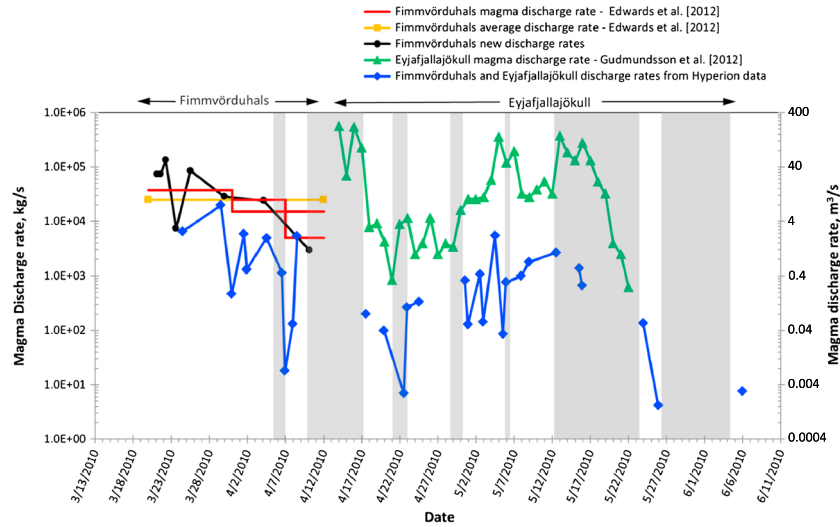


Figure 15. Magma discharge rates for Fimmvörðuháls and Eyjafjallajökull as derived from Hyperion data (blue diamonds) compared with daily average estimates from ground-based observers. The areas between the red lines show the uncertainty in the *Edwards et al.* [2012] estimates. The black circles show new estimates of effusion rate based on the *Edwards et al.* [2012] areal coverage rates shown in Figure 11d. Gray areas represent times when *EO-1* observations were hampered by clouds. A dense rock equivalent (DRE) of 2500 kg/m^3 is used to convert mass erupted to volume erupted.

emission. There is a relatively low level of thermal emission (and, by inference, effusion rate) on 7 April 2010 followed by a sharp increase on 8 April 2010, when estimated effusion rate was as high as it had been 4 days earlier. This was the last Hyperion observation of effusive activity at Fimmvörðuháls.

7.2. Fimmvörðuháls: Comparison With Ground-Based Estimates

[53] We now compare effusion rate derived from Hyperion data with estimates made in the field. It is possible to calculate the volume erupted during an effusive or explosive eruption after the event is over by examining the extent and thickness of new lava flows and the distribution and volume of volcanic ash deposits, but estimating effusion rate during

an ongoing eruption is difficult. For example, mapping the extent and thickness of active lava flows is potentially hazardous, and it is not always possible to remain in place to measure flow inflation. Post-eruption, the total volume erupted at Fimmvörðuháls was determined to be $20 \times 10^6 \text{ m}^3$. [*Gudmundsson et al.*, 2012]. *Edwards et al.* [2012] estimated mean effusion rates of $15 \text{ m}^3/\text{s}$ between 20 and 31 March 2010, $6\text{--}10 \text{ m}^3/\text{s}$ between 31 March and 7 April 2010, and $2\text{--}6 \text{ m}^3/\text{s}$ between 7 and 12 April 2010. These effusion rates are shown in Figure 15.

[54] Also shown in Figure 15 are updated estimates of effusion rate at a higher temporal resolution using the *Edwards et al.* [2012] map of changing areal coverage by lava flows (Figure 11d). Even on the sampling time scales,

broad swings in activity were seen, consistent with a dynamic, rapidly changing eruption. We use an average flow thickness of 15.4 m, determined from field measurements. The fit of an effusion rate change profile to the data is constrained by the total volume erupted (0.020 km^3). The effusion rate derived from the *Edwards et al.* [2012] data reached a peak of $49 \text{ m}^3/\text{s}$ on 22 March 2010 and dropped sharply to $2.7 \text{ m}^3/\text{s}$ on 24 March 2010. This apparent drop in effusion rate was probably the result of thickening of the lava flow field by inflation, when lateral growth of the flow field was limited. Effusion rate subsequently increased to $31 \text{ m}^3/\text{s}$ on 26 March 2010, before decreasing, tailing off, and stopping entirely by 13 April 2010.

[55] The Hyperion-derived effusion rates broadly mirror the time-averaged effusion rates from ground-based flow mapping, but underestimate effusion rate in most cases by an order of magnitude. This is because, firstly, the methodology used to estimate total thermal emission (a single-temperature fit to the spectrum of each pixel) is not necessarily the best method for an eruption of this type. Whereas this method has been shown to provide robust radiant fluxes for an active, overturning lava lake [*Davies et al.*, 2008a], active lava flows like those emplaced at Fimmvörðuháls have a wider and more complicated surface temperature distribution that is best fitted with a more sophisticated thermal emission model involving two or more temperature components. Secondly, it is not possible to detect flow inflation in Hyperion data, leading to further underestimation of actual effusion rate from Hyperion radiance data alone. Thirdly, we are comparing (ground-based) estimated time-averaged eruption rates with instantaneous effusion rate estimates (derived from space) during a dynamic, rapidly changing eruption.

7.3. Eyjafjallajökull Effusion Rate Estimates (14 April to 22 May 2010)

[56] Eruption rates during the Eyjafjallajökull eruption were estimated from radar-derived plume heights using the methodology of *Mastin et al.* [2009] scaled with measured fallout on the ground [*Gudmundsson et al.*, 2012]. These results are also shown in Figure 15 and are also given in kilogram per second using a dense rock equivalent (DRE) of 2500 kg/m^3 . Daily average effusion rates rapidly reached a peak of $230 \text{ m}^3 \text{ s}^{-1}$ ($\sim 6 \times 10^5 \text{ kg s}^{-1}$) on 14 April 2010, the first day of this eruption. This episode was most active in terms of volumetric discharge between 14 and 17 April 2010, with discharge rates on 16 and 17 April 2010 of 220 and $90 \text{ m}^3/\text{s}$. Effusion rates exceeded $50 \text{ m}^3/\text{s}$ again on 5 May 2010 ($140 \text{ m}^3/\text{s}$), 7 May 2010 ($80 \text{ m}^3/\text{s}$), 13 May 2010 ($150 \text{ m}^3/\text{s}$), 14 May 2010 ($70 \text{ m}^3/\text{s}$), 15 May 2010 ($50 \text{ m}^3/\text{s}$), and 16–17 May 2010 (110 and $50 \text{ m}^3/\text{s}$) (based on *Gudmundsson et al.* [2012]).

[57] Hyperion-derived effusion rates (Table 3 and Figure 15), which are estimated from measurements of thermal emission, are not directly applicable to eruptions such as the explosive, plume-producing phases of the Eyjafjallajökull eruption. The amount of thermal energy seen at short-infrared wavelengths is greatly reduced by optically thick eruption plumes of the type encountered at Eyjafjallajökull. In addition, an important mechanism influencing the eruption plume, at least during the first explosive phase, is the thermal exchange between hot lava and melting glacial ice. Thermal energy (the sensible and latent heat content of the lava) firstly melts ice and heats water to steam—this is a highly energetic process that results in

rapid, violent expansion of gases and the entrainment of ash fragments to form a rapidly ascending, convecting ash plume. Thermal energy is converted into mechanical energy, and Hyperion is not sensitive to this process. As a result, Hyperion-derived effusion rates underestimate actual effusion rate by an order of magnitude or more. However, as with the Fimmvörðuháls eruption, the Hyperion thermal emission data do, generally, follow the effusion rate trends revealed in the Eyjafjallajökull eruption rate timeline derived from charting plume height.

8. MODIS Observations of Thermal Emission

[58] Figure 14 shows the variability of power output from Fimmvörðuháls and Eyjafjallajökull, as derived from Hyperion data (see Table 3). Shaded areas are where observations were significantly affected by cloud. Also shown are estimates of thermal emission derived from data collected by the MODIS instrument on *Terra* and *Aqua* at night. Thermal emission as detected by MODIS is generally consistent with that seen by Hyperion during the Eyjafjallajökull 2010 eruption, and fills in some of the gaps in the Hyperion timeline. The thermal detection algorithm used to process MODIS data relies on data at short wavelength infrared (SWIR) and thermal infrared (TIR $\sim 12 \mu\text{m}$) wavelengths [*Wright et al.*, 2002; *Wright et al.*, 2004]. MODIS is sensitive to thermal emission from (typically) larger and cooler surfaces, so it is unsurprising that MODIS-derived radiances are commonly larger than those derived solely from visible to short wavelength infrared (VIS-SWIR) Hyperion data using single-temperature fits. Exceptions to this relationship occur when all of the thermal sources present are at relatively high temperatures. In these cases, short-wavelength thermal emission detected by Hyperion is greater than that at longer wavelengths, detected by MODIS.

9. Discussion

[59] *EO-1* obtained 50 pairs of observations (Hyperion and ALI) of this eruption in less than 3 months, an unprecedented frequency for such high spatial resolution space-based imagers. The high observation frequency was only possible as a result of *EO-1* operational streamlining as a result of implementing ASE-type automatic mission planning. The Volcano Sensor Web enabled the rapid generation and posting of data products. The VSW is a template for future space missions, utilizing automated systems and data processing to maximize science return.

[60] A comparison of estimates of effusion rate reveals some of the limitations of techniques on the ground and those applied to remote-sensing data. Hyperion data allow an estimation of instantaneous effusion rate, but this is, in most cases and using this methodology, a minimum value by at least an order of magnitude. The Fimmvörðuháls effusion rate was derived from maps of lava flow coverage and used a post-eruption estimate of volume erupted to estimate an average flow thickness. These data allow daily average effusion rates to be calculated, but only after the eruption has halted.

[61] Similarly, a number of observations of plume height were used to estimate daily average effusion rate at Eyjafjallajökull. Comparisons are therefore being made between instantaneous observations and daily averages; it

is therefore not possible to say with great certainty by how much our approach to Hyperion data processing underestimates effusion rate.

[62] The only solution to this problem, and to ensure a robust comparison and enable future refinement of data processing models as a result, is to ensure that ground-based observations of plume height, extent of activity (in the case of lava flows), and style of volcanic activity are obtained simultaneously with space-based observations. This synchronicity has been achieved a number of times before with Hyperion at Erebus (Antarctica), Erta'Ale (Ethiopia), and Kilauea (US) volcanoes [e.g., Davies *et al.*, 2008a; 2011].

[63] Some Icelandic volcanologists were informed in advance that EO-1 observations were to be obtained, but these data were not often relayed to workers in the field so that they could note precise eruption behavior at the time of observation (plume height, lava flow dimensions, and/or style of activity). Part of the problem was that personnel monitoring the eruption were already extremely busy. Another part of the problem was that people were unaware of the capabilities of the EO-1 instruments and the detail of the resulting images. The usefulness of these data became apparent only after the eruption, when the full capability of the VSW was realized. One useful outcome from this eruption was the exchange of information and discussions that highlighted the areas where further cooperation was desirable. One immediate spin-off was the integration of Icelandic Meteorological Office seismic sensors located on Iceland's volcanoes into the VSW (see Appendix B). For post-2010 eruptions, monitoring would be triggered by eruption precursors rather than a few days after the eruption starts.

[64] How useful were the VSW products during the Eyjafjallajökull eruption of 2010 to the decision makers, watching the eruption run its course? This is difficult to determine. Unlike the 2006 eruption of Nyamuragira [see Davies *et al.*, 2008b], where a spacecraft observation was the only way to determine vent location and subsequent lava flow direction, a lack of data was not a problem during the Eyjafjallajökull eruption. In Iceland, observers were in place on the ground very shortly after (within hours of) the start of the eruption. At present, satellite methods cannot replace the "near field" observations in terms of accuracy. However, remote-sensing observations are especially useful for detecting changes at night (lava flows changing direction, new vents, etc.) when other observations are unavailable. In these cases, rapid delivery of data and products (as demonstrated using the VSW) is very important for local observers.

[65] A second point is that observation of remote areas presently out of range of detailed monitoring is possible. The Hyperion observations of early May 2010 revealed that the lava flows moving to the north of the vent had removed all of the ice immediately above them, pointing to an imminent reduction in water flowing off the ice cap. While for the case of Eyjafjallajökull this was seen by observers on the spot, the capability of doing this remotely is of immense value for charting the course of inaccessible eruptions and evaluating the resulting hazards. A particular strength of this study is to determine the limitations of remote sensing and to pinpoint areas of weakness in the present volcano-observing method of operation.

[66] In summary, a number of lessons have been learned from the Eyjafjallajökull 2010 eruption:

[67] 1. *Effusion rates.* At Fimmvörðuháls, the comparison of eruption rate data sets is difficult because we are comparing time-averaged eruption rate ground-based data with instantaneous effusion rates from a spacecraft.

[68] 2. *Communications.* Better communications of satellite overpasses to field workers is vital to enable precise timing of ground-based observations at the moment of spacecraft observations. This is particularly important with rapidly changing styles of activity.

[69] 3. *Field observations.* A higher frequency of ground-based observations is desirable in order to build up an effusion rate profile with a higher temporal resolution. Also desirable is the setting up of multiple vantage points, both manned and remote instrument stations, where possible, to chart the evolution of the eruption. Both visible and IR data are desirable. Repeated ground surveys are needed to chart flow field growth and degree of inflation. If the temporal resolution of ground-based observations of lava flow emplacement (areal extent, rate of change of area, flow thickness, and degree of inflation) could be improved to an interval of a few hours rather than a few days, more robust estimates of effusion rate and rate variability could be generated that would provide robust ground truth for testing the limits of models of effusion rate from remote-sensing data.

[70] 4. *Modeling.* Regarding the VSW, fitting Hyperion data or any other hyperspectral or multi-spectral imager data with more sophisticated temperature/area distribution models (at least a two-temperature model) will improve estimation of radiant flux and total heat loss and therefore a better estimation of effusion rate.

9.1. Future Plans for the VSW

[71] A major objective for the VSW is to obtain high temporal resolution spacecraft coverage of an eruption from a time before surface activity begins (see Appendix B). The goal is to chart the waxing phase of an episodic eruption to its peak and, as the eruption begins to wane, provide estimates of likely duration and total volume erupted. This could be accomplished using a model of exponential decay in effusion rate with time, linked to the release in elastic strain in the crust surrounding the magma chamber supplying the eruption [e.g., Wadge, 1981]. At the same time, the location of activity is provided for other users to forecast, in the case of lava flows, the likely direction and distance traveled [e.g., Wright *et al.*, 2010].

10. Conclusions

[72] The NASA Volcano Sensor Web links notifications of volcanic activity to a system that can retask the EO-1 spacecraft to observe the volcano of interest. The VSW demonstrates an autonomy-driven, multi-asset, spacecraft retasking and data processing system that maximizes science return by focusing on events of greatest interest and by extending missions through the most effective use of resources. Because the system is autonomous, it is fast and operates around the clock.

[73] The 2010 eruption of Eyjafjallajökull volcano, Iceland, was one of the most closely studied eruptions of recent years because of the effect the eruption had on air transportation worldwide. Using a spacecraft command and control system and resource manager capable of fully

autonomous operation, an unprecedented sequence of observations was obtained by *EO-1*. These observations revealed the different phases of the eruption, as lava fountains emplaced lava flows; the eruption moved under an ice cap, leading to an explosive eruption; and how new lava flows cut their way through the ice cap.

[74] Although the effusion rates generated by the VSW are almost certainly underestimations, the relative radiant fluxes measured and the distribution of hot pixels detected reveal considerable detail as to the style of volcanic activity. In conjunction with the high spatial resolution of the data (10 to 30 m), these images allow pinpointing of vents and lava flows, as well as producing data that can be used to estimate plume height from measurement of plume shadow height.

[75] The increased efficiency of the autonomous system of resource allocation and spacecraft retasking and the delivery of information vital to mitigating volcanic risk and hazard was demonstrated most impressively at Nyamuragira volcano in 2006, and the speed of response enabled by linking in situ sensors to spacecraft was demonstrated during the

Grímsvötn volcano eruption of May 2011. Streamlining of spacecraft operations—that is, the task of requesting and changing what the spacecraft is required to do—is now so simple that inserting new observations is a matter of a few key strokes. This ease of operation led to the unprecedented and unique sequence of observations obtained of the 2010 eruption of Eyjafjallajökull. This was a compelling demonstration of how the VSW, by combining alerts from multiple sources with advanced autonomy to handle resources and process data, is a template for operating future NASA missions to extract the highest possible science return [e.g., Chien *et al.*, 2010b]. It is hoped that the VSW can repeat this effort with other eruptions in more remote locations (e.g., parts of Alaska, Kamchatka, Indonesia, South America) that have the potential to cause similar problems as Eyjafjallajökull.

Appendix A: ASE and VSW Automatically Generated Products From *EO-1* Data

Table A1. ASE and VSW Automatically Generated Products From *EO-1* Data

Instrument	ID	Product	Description
Basic Hyperion product processing			
Hyperion	1.1	L0 data and browse image	Raw, unprocessed radiance data
Hyperion	1.2	L0.5 data and browse image	Radiance product processed on <i>EO-1</i> by ASE. See Doggett <i>et al.</i> [2006]
Hyperion	2	L1R data and browse image	Radiometrically corrected radiance data (Figure 4)
Hyperion	3	L1G data and browse image	Geolocated data (Figures 11b and 11c)
Hyperion bands			
Hyperion	4.1	Band 110 (1.245 μm) image	Used by ASE THERMAL_CLASSIFIER (see section 6; Davies <i>et al.</i> [2006a]) (Figure 4)
Hyperion	4.2	Band 150 (1.649 μm) image	Used by ASE THERMAL_CLASSIFIER (Figure 7a)
Hyperion	4.3	Band 213 (2.285 μm) image	Used by ASE THERMAL_CLASSIFIER (Figure 7a)
ASE data processing			
Hyperion	5.1	Hot pixel locations	Map showing line, sample of each hot pixel (Figure 7a) detected using ASE THERMAL_CLASSIFIER
Hyperion	5.2	Temperature map	Map of temperatures fitted to spectra of selected pixels
Hyperion	5.3	Pixel fraction map	Pixel fraction occupied by thermal source at fitted temperature (ID 5.1)
VSW data processing			
Hyperion	6.1	Hyperion L1R radiance spectrum	Spectrum for each hot pixel (ID 5.1, 5.2) (blue curve, Figures 8 and 9) corrected for emission angle and range to target
Hyperion	6.2	Saturated bands	Saturated bands, not used for temperature fitting (gray area, Figure 9)
Hyperion	6.3	Corrected L1R radiance spectrum	Sunlight component removed; corrected for atmospheric absorption (black line, Figures 8 and 9)
Hyperion	6.4	Thermal blackbody fit	Single-temperature fit to unsaturated data (green curve, Figures 8 and 9)
Results for each detected hot pixel			
Hyperion	7.1	Temperature (best-fit)	Text file: Single-temp. best fit to unsaturated data (K)
Hyperion	7.2	Pixel fraction filled by thermal source	Text file: Fraction of pixel filled by thermal source (m^2)
Results for entire scene			
Hyperion	8.3	Q_{rad} Radiant power (W)	Table 2
Hyperion	8.4	Q_{conv} Convective heat loss (W)	Table 2
Hyperion	8.5	$Q_{\text{rad}} + Q_{\text{conv}}$ Total energy loss (W)	Table 2
Hyperion	8.6	Q_F effusion rate estimate ($\text{m}^3 \text{s}^{-1}$)	Table 2; also expressed as kg s^{-1}
Hyperion	8.7	Total emitting area (m^2)	Table 2; sum of all areas in ID 7.2
Time history			
Hyperion	9	Time history, chart, and .csv file	Plot of Q_{TOT} with time (using all available observations). The .csv file is easily imported into a display program such as Microsoft Excel (Figure 14).
ALI products			
ALI	10.1	L1R product	Radiometrically corrected radiance product (Figure 5, SWIR bands)
ALI	10.2	L1G product	Geolocated product (Figures 6a and 11c)
ALI	10.3	Thumbnail image	Created from visible wavelength L1G data

Appendix B: IMO-VSW Linkage and the Grímsvötn Volcano, Iceland, 2011 Eruption

[76] Eyjafjallajökull 2010 was not imaged by *EO-1* until 3 days after the eruption began because VSW triggering was based on notification of the ongoing eruption from a non-VSW (i.e., non-autonomous) source—in this case, from broadcast news reporting. MODVOLC, Volcanic Ash Advisory Centres (VAAC), and US Air Force Weather Agency (AFWA) alerts soon followed after 21 March 2010. In order to get a better response for future Iceland eruptions, a link was initiated between the Icelandic Meteorological Office (IMO) ground-based sensors and the VSW in June 2010.

[77] The VSW is now linked to the Icelandic Meteorological Office SIL (South Iceland Lowland project) seismic network [Böðvarsson *et al.*, 1996]. The VSW retrieves SIL data via a derived product that is updated approximately every 5 min in Iceland [Kjartansson, 1997]. Earthquake hypocenters are calculated for seismic events across Iceland [Böðvarsson *et al.*, 1999]. A VSW software agent (a computer program) examines these data approximately every 30 min and computes an energy-time-density function. For each new hypocenter, the system captures all preceding hypocenters and calculates the sum of the event magnitudes, modifying each magnitude using exponential decays of time and distance to the current event location. Sums exceeding a predetermined threshold are deemed triggers if they lie within some radius (currently 10 km) of a known target. That target is used for a sensor web request retasking *EO-1*.

[78] The triggering algorithm works as follows. If

T = time constant in seconds (currently $5 * 3600 = 5$ h), and
 D = distance constant (currently 8 km)
 e_0 = most recent event

[79] and

Ae = all events preceding e_0 within $10 T$

[80] for a single event i

e_i = single event in Ae
 d_i = distance from e_i to e_0 (km)
 t_i = time separation from e_i to e_0

[81] and

m_i = magnitude of event e_i

[82] then

$$j_i, \text{ the approximate magnitude of event } e_i = 10^{(m_i/10)}; \quad (4)$$

and

$$Ft_i, \text{ the time falloff factor,} = 1 / \left(1 + 10^{(3(t_i - T)/T)} \right); \quad (5)$$

and

$$Fd_i, \text{ the distance falloff factor,} = 1 / \left(1 + 10^{(3(d_i - D)/D)} \right). \quad (6)$$

[83] The situation “score,” X , is given by

$$X = 10 \log_{10} \sum_{i \in Ae} (j_i Ft_i Fd_i) \quad (7)$$

and an alarm is generated if

$$X > \text{threshold} \quad (8)$$

[84] The variable threshold value was set by testing this algorithm out on historical data, particularly the Eyjafjallajökull 2010 eruption. Initially, a threshold of 5 was used. The threshold has been varied a number of times to fine-tune the system reaction. Since June 2010, the threshold has been set at 8. To prevent a flood of alerts as might arise from an earthquake swarm, once activity crosses the threshold, triggering is suppressed for a future window of time that rolls forward with over-threshold activity; for each new event, any prior event within the distance falloff factor cutoff $Fd_i > 10^{20}$ (~61 km), within $10 T$ (50 h), and exceeding the threshold (regardless of whether that event generated a trigger) will suppress a new trigger: things need to quiet down for ~50 h within a ~61 km radius before triggering another alert.

[85] These triggers result in a message that is sent to the Science Event Manager (SEM) and processed through a campaign per the usual sensor web route described above. In the message-generation process, the alert’s geographic location is compared to a database of observation targets throughout the region. The nearest of all targets within 60 km is associated with the event, and the target’s geographic location is used to point the *EO-1* observation. If there are no targets with the search radius, the message is not sent to the SEM, but an email is sent instead to the VSW team. There are several reasons for this: (a) simple organizational benefit—to associate the observation with well-known geographic features; (b) to filter areas of common seismic activity but little volcanic activity; and (c) to minimize scattering of observation pointing that would occur from following the noisy hypocenter locations and anchor on well-known surface features. This approach poses some risk of missing an observation through inaccurate pointing via alterations in volcanic surface expression or completely dropping legitimate triggers for not having an existing target prepared in the database. However, the alternative approach had been tested, and the current approach is preferred—repeated triggering events had been generated in the Reykjanes Peninsula and off the north coast of Iceland, none of which would have been valuable observations to the VSW.

[86] As a preemptive measure before the next inevitable eruption in Iceland, baseline images of areas likely to be inundated by jökulhaups during a large eruption of Grímsvötn or Bárðabunga were obtained by ALI and Hyperion in the summer of 2010.

[87] On 21 May 2011, shortly before 18:00 UT, a seismic swarm was detected at Grímsvötn volcano. Within 20 min of the onset of seismic activity, the VSW had received an alert, and the VSW requested an *EO-1* observation. Unfortunately, observations obtained by *EO-1* over the next 2 weeks (24 and 25 May 2011 and 4, 7, and 11 June 2011) were heavily impacted with cloud, although partial images of Mýrdalsjökull may prove useful for estimating ash coverage. This was a VEI 4 eruption, considerably larger than the one at Eyjafjallajökull a year earlier (Institute of Earth Sciences, unpublished data).

Sent: Monday, September 05, 2011 10:34 AM
 Subject: iceland alert alarm. sem response: 200 OK sem response: 200 OK sem URL:
 http://eo1fs.jpl.nasa.gov/ port: 2222 sem response: 200 OK

```

    accumulated value: 8.46811
    gmt, j2ksec, date, t, lat, lon, depth, mag, qual, idxperday
    1315243771.2||368515771.20000005||'2011-09-
    05' || '17:29:31.2' || 63.643999999999998 || -
    19.050999999999998 || 4.0 || 1.600000000000001 || 'B' || 68
  
```

--- POST TO SEM FOLLOWS ---

```

<ScienceAlert>

<EventTime>1315243771</EventTime>

<ExpirationDate>1315589371</ExpirationDate>

<Source>
  <Name>ICELAND_VEDUR_EQ</Name>
  <AgentID>21</AgentID>
</Source>

<EventType>
  <Phenomenon>VOLCANIC</Phenomenon>
  <Class>0</Class>
</EventType>

<Target>
  <Name>Katla</Name>
  <Coordinates>
    <Latitude>63.630000</Latitude>
    <Longitude>-19.050000</Longitude>
    <Precision>0.001000</Precision>
  </Coordinates>
</Target>

<Priority>500</Priority>

<Attributes>
  <triggertype>earthquake accumulator</triggertype>
  <val>8</val>
  <depth>4.000000</depth>
  <magnitude>1.600000</magnitude>
  <comment>From the alert.mag data stream</comment>
  <j2ksec>3.685158e+08</j2ksec>
  <qual>B</qual>
  <idxperday>68</idxperday>
  <targetdist>1.554665</targetdist>
</Attributes>

</ScienceAlert>
  
```

As a result of the VSW activity above, the following notification was automatically sent by email

by the VSW to a list of interested persons:

```

-----
From: ASE Operations
Sent: Monday, September 05, 2011 10:37 AM
To: [ASE users]
Subject: EO-1 replacement for DOY 250
  
```

The following replacement scene has been queued for uplink:

```

Katla [SW/E4] JPL 2011-250/11:54:26 392 63.63 -19.05 [ICELAND_VEDUR_EQ 2011-
248/17:29:31] (id=608886)
  
```

[88] As another example, on 5 September 2011 a cluster of seismic events at Katla volcano generated another trigger that resulted in an observation by *EO-1*. The following text shows the form of the trigger (“accumulated value”) and the relevant parameters and the information passed to the SEM, including

the source of the trigger, the event type, the target information, the priority of the request, and the attributes of the trigger.

[89] This is the style of notifications that generally appear a few times a week. In this case, the seismic network monitoring Katla volcano, Iceland, had measured seismic activity

that exceeded the trigger threshold described above. This triggered VSW notification, and the system automatically inserted an EO-1 observation request that was accepted by the planner. The observation was obtained on Wednesday, 7 September 2011 at 11:54 UT. No volcanic activity was detected. The seismic activity was probably a flood-induced tremor but demonstrated the usefulness of the system prior to the next, inevitable eruption of an Icelandic volcano.

[90] **Acknowledgments.** This work was performed at the Jet Propulsion Laboratory, California Institute of Technology, under contract to NASA. © 2013 Caltech. All rights reserved. *Earth Observing 1* is managed by the NASA Goddard Space Flight Center, Greenbelt, Maryland, USA. T. Thordarson's contribution to this project was supported by NERC Emergency Grant (Ne/I00775x/1). The authors thank Michael Ramsey, Gaetana Ganci, and David Rothery for their detailed and extremely useful reviews of the manuscript, and Alison Canning Davies for her meticulous review of the proofs.

References

- Aster, R., et al. (2004), Real-time data received from Mount Erebus Volcano, Antarctica, *EOS Trans.*, **85**, 97–101.
- Beck, R. (2003), *EO-1 User Guide*, Version 2.3, University of Cincinnati, Dept. of Geography, available from <http://eo1.usgs.gov>.
- Böðvarsson, R., S. T. Rögnvaldsson, S. S. Jakobsdóttir, R. Slunga, and R. Stefánsson (1996), The SIL data acquisition and monitoring system, *Seismol. Res. Lett.*, **67**, 35–46.
- Böðvarsson, R., S. T. Rögnvaldsson, R. Slunga, and E. Kjartansson (1999), The SIL data acquisition system—At present and beyond year 2000, *Phys. Earth Planet. Inter.*, **113**, 89–101.
- Boudreau, K., J. R. Cecava, A. Behar, A. G. Davies, D. Tran, D. C. Pieri, and A. Abtahi (2007), Autonomous triggering of *in situ* sensors on Kilauea Volcano, HI from eruption detection by the EO-1 Spacecraft: Design and operational scenario, *Eos Trans. AGU*, **88**(52), *Fall Meet. Suppl.*, Abstract V11C-0753.
- Cervelli, P. F., and A. Miklius (2003), The Shallow Magmatic System of Kilauea Volcano, in *The Pu'u 'O'o-Kupaianaha Eruption of Kilauea Volcano, Hawai'i: The First 20 Years*, edited by C. Heliker, et al., pp. 149–164, U.S. Geological Survey Professional Paper 1676.
- Chien, S., et al. (2005a), An autonomous Earth-observing SensorWeb, *IEEE Intell. Syst.*, **20**(3), 16–24.
- Chien, S., et al. (2005b), Using Autonomy Flight Software to improve science return on *Earth Observing One*, *J. Aerosp. Comput. Inf. Commun. AIAA*, **2**(4), 196–216.
- Chien, S., R. Doyle, A. G. Davies, A. Jónsson, and R. Lorenz (2006), The future of AI in space, *IEEE Intell. Syst.*, **21**(4), 64–69.
- Chien, S., et al. (2010a), A multi-agent space, *in situ* Volcano SensorWeb, *International Symposium on Space Artificial Intelligence, Robotics, and Automation for Space (iSAIRAS 2010)*.
- Chien, S., D. Silverman, A. G. Davies, D. McLaren, D. Mandl, and J. Hegemihle (2010b), Onboard instrument processing concepts for the *HyspIRI* Mission, *Proc. IGARSS 2010, Honolulu, HI, July 2010*, 3784–3751.
- Chien, S., J. Doubleday, D. McLaren, A. G. Davies, D. Tran, V. Tanpipai, A. Ratanasuwan, and D. Mandl (2011), Space-based sensorweb monitoring of wildfires in Thailand, *IGARSS 2011, Proc. Intl. Geosci. Remote Sens. Symp.*, Vancouver, BC, Canada, July 2011.
- Davies, A. G., et al. (2006a), Monitoring active volcanism with the autonomous Spacecraft Experiment on EO-1, *Remote Sens. Environ.*, **101**(4), 427–446.
- Davies, A. G., S. Chien, R. Wright, A. Miklius, P. R. Kyle, M. Welsh, J. B. Johnson, D. Tran, S. R. Schaffer, and R. Sherwood (2006b), Sensor Web enables rapid response to volcanic activity, *Eos*, **87**(1), 1 & 5.
- Davies, A. G., J. Calkins, L. Scharenbroich, R. G. Vaughan, R. Wright, P. Kyle, R. Castaño, S. Chien, and D. Tran (2008a), Multi-instrument remote and *in situ* observations of the Erebus Volcano (Antarctica) Lava Lake in 2005: A comparison with the Pele Lava Lake on the Jovian Moon Io, *J. Volcanol. Geotherm. Res.*, **177**(3), 705–724.
- Davies, A. G., R. Castaño, S. Chien, D. Tran, L. Mandrake, R. Wright, P. Kyle, J.-C. Komorowski, D. Mandl, and S. Frye (2008b), Rapid response to volcanic eruptions with an autonomous Sensor Web: The Nyamulagira eruption of 2006, in *Proc., IEEE Aerospace Conference*, edited, Big Sky, Montana, March 2008.
- Davies, A. G., et al. (2008c), The model-based Volcano Sensor Web: Progress in 2007, *NASA Earth Science and Technology Conference, Adelphi, MD, paper A7P3*, 20–24 June 2008, http://esto.nasa.gov/conferences/estc2008/papers/Davies_Ashley_A7P3.pdf.
- Davies, A. G., L. Keszthelyi, and A. S. McEwen (2011), Estimating eruption temperature from thermal emission spectra of lava fountain activity in the Erta' Ale (Ethiopia) Volcano Lava Lake—Implications for observing Io's volcanoes, *Geophys. Res. Lett.*, **38**, L21308.
- Doggett, T., et al. (2006), Autonomous detection of cryospheric change with Hyperion on-board *Earth Observing-1*, *Remote Sens. Environ.*, **101**(4), 447–462.
- Edwards, B., M. T. Gudmundsson, T. Thordarson, E. Magnússon, A. Höskuldsson, and J. Haklar (2012), Interactions between snow/firn/ice and lava/tephra during the 2010 Fimmvörðuháls eruption, south-central Iceland, *J. Geophys. Res.*, **117**(B04302).
- Glaze, L., L. Wilson, and P. Mougini-Mark (1999), Volcanic eruption plume top topography and heights as determined from photoclinometric analysis of satellite data, *J. Geophys. Res.*, **104**, 2989–3001.
- Gudmundsson, M. T., et al. (2012), Ash generation and distribution from the April–May 2010 eruption of Eyjafjallajökull, Iceland, *Sci. Rep.*, **2**(572), 12 pages, doi:10.1038/srep00572.
- Harris, A. J. L., L. Keszthelyi, L. P. Flynn, P. J. Mougini-Mark, C. Thornber, J. Kauahikaua, D. Sherrod, F. Trusdell, M. W. Sawyer, and P. Flament (1997), Chronology of the episode 54 eruption at Kilauea Volcano, Hawaii, from GOES-9 satellite data, *Geophys. Res. Lett.*, **24**, 3281–3284.
- Harris, A. J. L., L. P. Flynn, D. A. Rothery, C. Oppenheimer, and S. B. Sherman (1999), Mass flux measurements at active lava lakes: Implications for magma recycling, *J. Geophys. Res.*, **104**(B4), 7117–7136.
- Harris, A. J. L., and C. Thornber (1999), Complex effusive events at Kilauea as documented by the GOES satellite and remote video cameras, *Bull. Volcanol.*, **61**(6), 382–395.
- Ip, F., et al. (2006), Flood detection and monitoring with the autonomous Spacecraft Experiment onboard EO-1, *Remote Sens. Environ.*, **101**(4), 463–481.
- Kjartansson, E. (1997), Monitoring volcanic tremor in Iceland, *Abstract 6509, AGU Fall Meeting, San Francisco, California, 8–12 December*.
- LaHusen, R., et al. (2010), Design and performance of an integrated ground and space sensor web for monitoring active volcanoes, in *EGU General Assembly, Vienna, Austria, 2–7 May 2010, Abstract EGU2010-12750*, edited.
- Larsen, G. (1999), Gosið í Eyjafjallajökli 1821–23. Stutt samantekt á framvindu og áhrifum gossins samkvæmt lýsingum [The eruption of Eyjafjallajökull 1821–23. A short summary of course of events and effects based on contemporary accounts], *RH-28-99, 14 pp.*, *Sci. Inst., Reykjavik*.
- Magnússon, E., M. T. Gudmundsson, G. Sigurdsson, M. J. Roberts, F. Höskuldsson, and B. Oddsson (2012), Ice-volcano interactions during the 2010 Eyjafjallajökull eruption, as revealed by airborne radar, *J. Geophys. Res.*, **117**, B07405, doi:10.1029/2012JB009250.
- Mastin, L. G., et al. (2009), A multidisciplinary effort to assign realistic source parameters to models of volcanic ash-cloud transport and dispersion during eruptions, *J. Volcanol. Geotherm. Res.*, **186**, 10–21.
- Óskarsson, B. (2009), The Skerín ridge of Eyjafjallajökull, south Iceland: Morphology and magma-ice interaction in an ice-confined silicic fissure eruption, 111 pp, M.Sc. Thesis, Faculty of Earth Sciences, University of Iceland, Reykjavik.
- Pearlman, J. S., P. S. Barry, C. C. Segal, J. Shepanski, D. Beiso, and S. L. Carman (2003), Hyperion, a space-based imaging spectrometer, *IEEE Trans. Geosci. Rem. Sens.*, **41**, 1160–1172.
- Sigmundsson, F., et al. (2010), Intrusion triggering of the 2010 Eyjafjallajökull explosive eruption, *Nature*, **468**, 426–430.
- Thordarson, T., and Á. Höskuldsson (2006), Iceland, 200 pp., Terra Publishing, Harpenden, Hertfordshire, UK.
- Thordarson, T., and G. Larsen (2007), Volcanism in Iceland in historical time: Volcano types, eruption styles and eruptive history, *J. Geodyn.*, **43**, 118–152.
- Thordarson, T., Á. Höskuldsson, O. Sigmarsson, M. Gudmundsson, E. Magnússon, and F. Sigmundsson (2011), The 20 March to 12 April basaltic Fimmvörðuháls flank eruption at Eyjafjallajökull volcano, Iceland: Course of events, *Geophys. Res. Abstr.*, **Vol 13**, EGU2011-12212, 2011, *EGU Gen Assembly 2011*.
- Tilling, R. (Ed.) (1989), Introduction and overview, in *Volcanic Hazards: A Short Course in Geology*, Vol. 1, AGU, Washington, D.C.
- Wadge, G. (1981), The variation of magma discharge during basaltic eruption, *J. Volcanol. Geotherm. Res.*, **11**, 139–168.
- Wright, R., L. Flynn, H. Garbeil, A. Harris, and E. Pilger (2002), Automated volcanic eruption detection using MODIS, *Remote Sens. Environ.*, **82**(1), 135–155.
- Wright, R., L. P. Flynn, H. Garbeil, A. J. L. Harris, and E. Pilger (2004), MODVOLC: Near-real-time thermal monitoring of global volcanism, *J. Volcanol. Geotherm. Res.*, **135**(1–2), 29–49.
- Wright, R., H. Garbeil, and A. G. Davies (2010), The cooling rate of some active lavas as determined using an orbital imaging spectrometer, *J. Geophys. Res.*, **115**, B06205, doi:10.1029/2009JB006536.